The Astrophysical Journal, 728:88 (20pp), 2011 February 20 doi:10.1088/0004-637X/728/2/88

ENVIRONMENTAL DEPENDENCE OF THE KENNICUTT–SCHMIDT RELATION IN GALAXIES

Nickolay Y. Gnedin[1,2,3] and Andrey V. Kravtsov[2,3,4]
[1] Particle Astrophysics Center, Fermi National Accelerator Laboratory, Batavia, IL 60510, USA; gnedin@fnal.gov
[2] Kavli Institute for Cosmological Physics and Enrico Fermi Institute, The University of Chicago, Chicago, IL 60637, USA; andrey@oddjob.uchicago.edu
[3] Department of Astronomy & Astrophysics, The University of Chicago, Chicago, IL 60637, USA
[4] Enrico Fermi Institute, The University of Chicago, Chicago, IL 60637, USA
Received 2010 July 6; accepted 2010 December 2; published 2011 January 25

ABSTRACT

We present a detailed description of a phenomenological H_2 formation model and local star formation prescription based on the density of molecular (rather than total) gas. Such an approach allows us to avoid the arbitrary density and temperature thresholds typically used in star formation recipes in galaxy formation simulations. We present results of the model based on realistic cosmological simulations of high-z galaxy formation for a grid of numerical models with varied dust-to-gas ratios and interstellar far-UV (FUV) fluxes. Our results show that both the atomic-to-molecular transition on small, tens-of-parsec scales and the Kennicutt–Schmidt (K-S) relation on large, kiloparsec scales are sensitive to the dust-to-gas ratio and the FUV flux. The atomic-to-molecular transition as a function of gas density or column density has a large scatter but is rather sharp and shifts to higher densities with decreasing dust-to-gas ratio and/or increasing FUV flux. Consequently, star formation is concentrated to higher gas surface density regions, resulting in steeper slope and lower amplitude of the K-S relation at a given $\Sigma_{\rm H}$, in less dusty and/or higher FUV flux environments. We parameterize the dependences observed in our simulations in convenient fitting formulae, which can be used to model the dependence of the K-S relation on the dust-to-gas ratio and FUV flux in semi-analytic models and in cosmological simulations that do not include radiative transfer and H_2 formation. Finally, we show that ionized gas can contribute a significant fraction of the total gas surface density in environments typical for high-redshift galaxies.

Key words: cosmology: theory – galaxies: evolution – galaxies: formation – methods: numerical – stars: formation

Online-only material: color figures

1. INTRODUCTION

Conversion of gas into stars is one of the major sources of uncertainty in modeling the formation of galaxies. This uncertainty reflects our incomplete understanding of the process of star formation both locally and on global scales. Traditionally, star formation is included in cosmological simulations and simulations of isolated galaxies by using simple phenomenological prescriptions that relate local rate of star formation to the local density of gas, with some additional criteria such as temperature and density thresholds for the gas to be eligible for star formation. The parameters of these prescriptions are chosen so that the empirical power-law relation between the surface density of star formation, $\Sigma_{\rm SFR}$, and the surface density of (hydrogen) gas averaged on kpc scales, $\Sigma_{\rm H}$, $\Sigma_{\rm SFR} \propto \Sigma_{\rm H}^n$ with $n \approx 1$–1.4 (Schmidt 1959; Kennicutt 1998; Bigiel et al. 2008) observed in $z \approx 0$ galaxies is reproduced (see, e.g., Schaye & Dalla Vecchia 2008 for a recent overview).

However, both theoretical considerations and observational evidence indicate that such an approach may miss some important environmental trends. For example, the relation between the local star formation recipe and the large-scale Kennicutt–Schmidt (K-S) relation is not trivial and depends on the density and thermal structure of the interstellar medium (ISM; Kravtsov 2003; Tassis 2007; Wada & Norman 2007; Robertson & Kravtsov 2008; Schaye & Dalla Vecchia 2008; Saitoh et al. 2008). This is because for a given large-scale gas surface density, the fraction of dense, star-forming gas is determined by the gas density distribution function, which, in turn, depends on the thermal state of the ISM (Wada & Norman 2001; Robertson & Kravtsov 2008). For the same reason, the global rate of star formation may be controlled by the rate with which dense gas is formed by the ISM, rather than by the assumed local efficiency of the gas (Saitoh et al. 2008). This implies that star formation parameters tuned to reproduce the empirical K-S relation in one situation (e.g., in controlled simulations of isolated disks; Springel & Hernquist 2003; Schaye & Dalla Vecchia 2008) may not reproduce this relation in galaxies with significantly different ISM density distributions.

In addition, there is a growing observational evidence that the K-S relation is more complex than previously thought (Heyer et al. 2004; Boissier et al. 2003; Bigiel et al. 2008). For example, instead of a well-defined surface density threshold at low $\Sigma_{\rm H}$ below which $\Sigma_{\rm SFR}$ drops to zero (Martin & Kennicutt 2001), observations indicate a continuous relation between star formation rate (SFR) and gas surface densities (Boissier et al. 2007) down to small $\Sigma_{\rm H}$, albeit with a steeper slope (e.g., Bigiel et al. 2008). Likewise, studies of individual dwarf galaxies, which typically have low gas surface densities ($\Sigma_{\rm H} \lesssim$ 10–20 $M_\odot$ pc^{-2}) throughout their disks, show that the K-S relation in such galaxies is generally characterized by a considerably steeper slope, $n \approx 2$–4, than the canonical value of 1.4 (Heyer et al. 2004; Bigiel et al. 2008; Verley et al. 2010). Moreover, a recent detailed study of the global star formation relation by Bigiel et al. (2008) shows that a single power law is in general a poor description of the K-S relation over the entire range of surface densities. Instead, the slope of the $\Sigma_{\rm SFR}$–$\Sigma_{\rm H}$ relation may vary from the steep values of $n \approx 2$–4 at $\Sigma_{\rm H} \lesssim 10\,M_\odot$ pc^{-2} to linear $n \approx 1$ at $\Sigma_{\rm H} \sim$ 10–100 $M_\odot$ pc^{-2} and then possibly steepening again to $n \approx 1.5$–2 at $\Sigma_{\rm H} \gtrsim 100\,M_\odot$ pc^{-2}.

Finally, the growing evidence indicates that in high-redshift galaxies ($z \gtrsim 3$) the K-S relation is significantly steeper and has

an order of magnitude lower amplitude at $\Sigma_{\rm SFR} \lesssim 100\,M_\odot$ pc^{-2} (Wolfe & Chen 2006; Rafelski et al. 2011; see also Figure 3 in Gnedin & Kravtsov 2010).

This complex behavior of the SFR density with the density of the neutral gas (H I+H_2) can be understood if star formation occurs only in the molecular gas (Robertson & Kravtsov 2008; Gnedin et al. 2009; Krumholz et al. 2009c; Pelupessy & Papadopoulos 2009; Gnedin & Kravtsov 2010). Indeed, detailed observations of nearby galaxies show that star formation correlates most strongly with the molecular gas (e.g., Wong & Blitz 2002; Bigiel et al. 2008), especially with the densest gas traced by HCN emission (Gao & Solomon 2004; Wu et al. 2005), while it only correlates weakly, if at all, with the density of atomic gas (Wong & Blitz 2002; Kennicutt et al. 2007; Bigiel et al. 2008). We can thus expect that the relationship between the SFR density and gas density $\Sigma_{\rm H} = \Sigma_{\rm H_2} + \Sigma_{\rm H\,I}$ (the K-S relation) varies depending on the molecular fraction of the gas $f_{\rm H_2} = \Sigma_{\rm H_2}/\Sigma_{\rm H}$.

Several factors may control the molecular fraction in the gas on different spatial scales. On small scales of individual molecular complexes, it is primarily the cosmic dust abundance and the interstellar FUV radiation that control the atomic-to-molecular transition (e.g., Elmegreen 1993; Krumholz et al. 2008; see Stahler & Palla; 2005 for pedagogical review). On larger ($\sim$ kpc) scales, the fraction of dense, molecular gas in a patch of gas of a given $\Sigma_{\rm H}$ is expected to depend on the density distribution of gas in that patch (e.g., Elmegreen 2002). The density distribution itself depends on thermodynamics of gas (see, e.g., Robertson & Kravtsov 2008) and metallicity, as more metal-rich gas may be more efficient in building regions of higher densities via radiative shocks arising in the highly turbulent medium of gaseous disks. The density probability density function (PDF) should also reflect the global dynamics of gas in galactic disks in general. For example, spiral density wave will compress the gas facilitating its cooling and conversion of atomic gas into molecular form. Likewise, large-scale instabilities seed the turbulence in the disk that can shape the global density PDF (Wada & Norman 2001; Elmegreen 2002; Kravtsov 2003; Krumholz & McKee 2005).

Although observational studies of environmental dependence of the K-S relation on gas metallicity, interstellar FUV radiation, and other properties of galaxies are in their early stages (e.g., Bigiel et al. 2008; Krumholz et al. 2009a; Rafelski et al. 2011), it is clear that such strong dependences can have important implications for our understanding of galaxy evolution (see discussion in Gnedin & Kravtsov 2010). For example, given that observations indicate that star formation in low-metallicity, high-UV flux environments of high-redshift galaxies is concentrated to significantly higher gas surface densities (Wolfe & Chen 2006; Rafelski et al. 2011), stars in these galaxies should be confined to the high surface density regions and should therefore be more resistant against dynamical heating in mergers. At the same time, the longer gas consumption timescales in lower density regions of high-z gaseous disks along with high accretion rate would keep them gas-rich and more resilient to mergers as well (e.g., Robertson et al. 2004, 2006; Springel & Hernquist 2005). This can help to resolve one of the major puzzles of hierarchical galaxy formation: prevalence of thin disks at low redshifts in the face of high merger rates at high redshifts.

It is thus important to explore potential effects and implications of the environmental dependence of the K-S relation for the evolution of galaxies. However, to capture the key physics responsible for this dependence in cosmological simulations of galaxy formation is challenging, because this requires high spatial resolution to model dynamics of ISM in the hierarchically forming galaxies, three-dimensional radiative transfer (RT) to model local UV radiation flux, and the formation of molecular hydrogen. The latter is mediated by dust grains, which catalyze H_2 formation and provide the initial key shielding from interstellar FUV radiation. This shielding allows buildup of molecular fraction sufficient for H_2 self-shielding, which in turn shapes the sharp transition of atomic-to-molecular gas.

Although fully self-consistent modeling of dust chemistry and H_2 formation is still far beyond reach, phenomenological model capturing the essential metallicity and UV flux dependence of molecular fraction can be used to model H_2 in self-consistent, high-resolution cosmological simulations (Gnedin et al. 2009; Gnedin & Kravtsov 2010). In this study, we present a detailed description of such H_2 formation model and local star formation prescription based on the density of molecular (rather than total) gas. We present results for a grid of numerical models with varied dust-to-gas ratios and interstellar FUV radiation fluxes and explore the dependence of atomic-to-molecular transition on small, molecular cloud scales, on these variables and the effect this dependence has on the K-S relation on large $\sim$ kpc scales. We parameterize the dependences observed in our simulations in convenient fitting formulae, which can be used to model the metallicity and UV flux dependence of the K-S relation in semi-analytic models and in cosmological simulations that do not include RT and H_2 formation.

2. COMPUTATIONAL APPROACH

Our computational approach consists of the following steps.

1. We use a snapshot from a fully self-consistent cosmological simulation run to redshift $z = 4$ as the initial condition for the set of "fixed ISM" simulations described in the next step. The cosmological simulation used a previous incarnation of our H_2 formation model (Gnedin et al. 2009) and is, therefore, not fully consistent in its physical model to the new H_2 formation model that we develop here. We address this inconsistency in step 3. We label this cosmological simulation as "cosmo I."
2. Starting from the $z = 4$ output of cosmological simulation, we perform a large set (35) of "fixed ISM" simulations. Each of these simulations has the amplitude of the radiation field in the Lyman–Werner band and the dust-to-gas ratio fixed to constant values everywhere in the computational domain. Such simulations can be considered as highly realistic isolated galaxy simulations, which include live dark matter halo and stellar disk, and also allow for self-consistent infall of fresh gas and galactic outflows. Each of the "fixed ISM" simulations is continued for 600 Myr to ensure that the memory of the initial condition is forgotten. We have indeed verified that the adopted value of 600 Myr is sufficient by comparing the final snapshot with the intermediate snapshot at 300 Myr. We also continued a small subset of all "fixed ISM" simulations to 1 Gyr and, again, found essentially identical results at 1 Gyr and 600 Myr snapshots.
3. The set of "fixed ISM" simulations allows us to develop the H_2 formation model and is used for all the results presented in this paper. In order to verify that the use of a not completely consistent cosmological simulation in step 1 does not compromise our results, we re-run the

fully self-consistent cosmological simulation from the very beginning, now using the H_2 formation model presented in the Appendix. Using a snapshot from that new cosmological simulation (dubbed "cosmo II") as a new initial condition, we re-run a subset of our "fixed ISM" simulations with this new, fully self-consistent initial condition. We found that none of our results change if we use either of the two sets of "fixed ISM" simulations.

In the following two subsections, we describe in detail the two cosmological simulations and "fixed ISM" simulations, respectively.

We underscore that all original results presented in this paper utilize only the "fixed ISM" simulations. The self-consistent "cosmo II" is the simulation used in Gnedin & Kravtsov (2010) to study the K-S relation in high-redshift galaxies.

Our approach relies on the assumption that our "fixed ISM" simulations present a reasonable model for the density and velocity structure of ISM of both high- and low-redshift galaxies because we compare our results to the data for $z = 0$ galaxies. Alternatively, this can be viewed as an assumption that the main difference for global SFRs between different galaxies is due to their differences in metallicity and UV field, not due to density and velocity structures. Although non-trivial, this assumption is reasonable if the density and velocity structure of the ISM is mainly determined by supersonic turbulence driven by gravitational instabilities. Nevertheless, the assumption is not yet convincingly tested at present and will need to be validated (or disproved) by higher resolution simulations and observational measurements.

2.1. Cosmological Simulations

Both cosmological simulations ("cosmo I" and "cosmo II") were run with Adaptive Refinement Tree (ART) code (Kravtsov 1999; Kravtsov et al. 2002; Rudd et al. 2008) and follow a Lagrangian region corresponding to five virial radii of a system, which evolves into a typical halo of an L_* galaxy ($M \approx 10^{12}\,M_\odot$) at $z = 0$. The mass resolution in the high-resolution Lagrangian region is $1.3 \times 10^6\,M_\odot$ in dark matter and the mass resolution in baryons varies from $\sim 10^3\,M_\odot$ to $\sim 10^6\,M_\odot$ depending on the cell size and density. The simulation reaches peak spatial resolution of 260 comoving pc (65 pc in physical units at $z = 3$). The Lagrangian region is embedded into a cubic volume of $6h^{-1}$ comoving Mpc on a side to model the tidal forces from the surrounding structures properly, but this outer region is resolved only coarsely with a uniform 64^3 grid. Cosmological simulations follow collapse of dark matter and gas self-consistently in a scale-free LCDM cosmology with $\Omega_M = 0.3$, $\Omega_B = 0.046$, $\sigma_8 = 0.9$, and $h = 0.7$.

In addition to gasdynamics, our simulations include three-dimensional RT of UV radiation from individual stellar particles formed during the course of the simulation using the OTVET approximation (Gnedin & Abel 2001). Inclusion of the RT is important because the local UV flux can set ionization and heating balance of gas and influence the abundance of molecular hydrogen, as we describe below and in the Appendix. Unlike the intergalactic medium (IGM) after reionization, which can be assumed to be optically thin to ionizing radiation, the dense ISM gas of simulated galaxies may well be opaque to ionizing photons of all but the nearest stars.

The simulations incorporate non-equilibrium chemical network of hydrogen and helium and non-equilibrium cooling and heating rates, which make use of the local abundance of atomic, molecular, and ionic species and UV intensity. This network includes the formation of molecular hydrogen both in the primordial phase and on dust grains. The abundances of the relevant atomic and molecular species are therefore followed self-consistently during the course of the simulation. The heating and cooling terms in the equation for the internal energy include all of the terms normally included in the simulations of first stars and in the ISM models, including cooling on metals. We describe all included reactions and heating/cooling processes in the Appendix (Section A.4). Figure 10 in the Appendix shows the net cooling rates for different metallicities and UV fields. One of the interesting features shown in this figure is that, contrary to what is usually assumed, updated rates of Glover & Abel (2008) for H_2-related cooling channels result in H_2 dominating cooling of gas at temperatures $T \lesssim 5000$ K over cooling due to atomic species, such as C II and O I.

A crucial component of all our simulations is a subgrid model for the formation of molecular hydrogen on dust and its shielding from the FUV radiation by cosmic dust and self-shielding. The model is calibrated against the observed column density dependence of atomic and molecular gas fractions in the Milky Way (MW), Large Magellanic Cloud (LMC), and Small Magellanic Cloud (SMC; see the Appendix). In particular, the model reproduces the metallicity dependence of the column density of the sharp transition from the atomic to fully molecular gas observed in the MW, LMC, and SMC.

The only difference between "cosmo I" and "cosmo II" simulations is that the former uses the form of the H_2 formation model described in Gnedin et al. (2009), while the latter uses the formulation of the model developed in this paper and presented in the Appendix.

2.2. "Fixed ISM" Simulations

Each "fixed ISM" simulation starts from a $z = 4$ snapshot from one of the two cosmological simulations, as explained in step 3 above. In each of these simulations, we fix the dust-to-gas ratio and the interstellar radiation field at 1000 Å to constant values and run the simulations for at least 600 Myr. A small subset of the simulations were continued until 1 Gyr to verify the independence of our results on the initial conditions.

While fixing the dust-to-gas ratio in the whole computational domain to a fixed value, we do not change the metallicity of the gas from the value produced self-consistently in the simulation. Setting, for example, the metallicity in the whole domain to solar would unreasonably increase cooling rates in the IGM, well outside the galactic disk that we attempt to model in the "fixed ISM" simulations, which would result in serious numerical artifacts (like a sudden increase in the accretion rate by a large factor).

The RT in all "fixed ISM" simulations is still followed with the OTVET approximation, except that the amplitude of the radiation field as a function of frequency returned by OTVET is scaled uniformly to achieve a fixed value of $J_{1000\,\text{Å}}$. Thus, the OTVET approximation in these simulations is used to compute the shape of the radiation spectrum, while its amplitude remains fixed. This is important, for example, for maintaining the ratio of ionized radiation to the radiation in the Lyman–Werner band similar to the one produced by sources with realistic stellar spectra.

All "fixed ISM" simulations reported in the subsequent sections of this paper incorporate the H_2 formation model described in the Appendix. During the calibration stage of model development, additional "fixed ISM" simulations were run that explored the parameter dependence of our phenomenological H_2

formation model. These test simulations were used exclusively for model development and are not reported in this paper.

Using "fixed ISM" simulations, we explore a grid of values of dust-to-gas ratio $D_{\rm MW}$ from 10^{-3} to 3 relative to the MW value. The variable $D_{\rm MW}$ scales the rate coefficient for the H_2 formation on dust R_D and the absorption cross section of dust in the Lyman–Werner band $\sigma_{\rm LW}$ to the values characteristic for the MW:

$$R_D \equiv D_{\rm MW} R_0; \quad \sigma_{\rm LW} \equiv D_{\rm MW}\sigma_0, \tag{1}$$

where $R_0 = 3.5 \times 10^{-17}$ cm^3 s^{-1} (Wolfire et al. 2008) and $\sigma_0 = 2 \times 10^{-21}$ cm^2 (Draine & Bertoldi 1996; Glover & Mac Low 2007a), respectively.

The normalization of the interstellar FUV flux at 1000 Å,

$$U_{\rm MW} \equiv J_{1000\,\text{Å}}/J_{\rm MW},$$

used throughout this paper, is also defined in units of the typical MW value $J_{\rm MW} = 10^6$ photons cm^{-2} s^{-1} sr^{-1} eV^{-1} (Draine 1978; Mathis et al. 1983). We explore the range of $U_{\rm MW}$ from 0.1 to 100 in our "fixed ISM" simulations.

The star formation model in our simulations closely follows the recipe 2 of Gnedin et al. (2009) with small numerical modifications. Namely, the rate of star formation in each computational cell with molecular fraction $f_{\rm H_2} \geqslant 0.1$ is evaluated as

$$\frac{d\rho_\star}{dt} = \epsilon_{\rm SF}\frac{\rho_{\rm H_2}}{\tau_{\rm SF}}, \tag{2}$$

where the timescale for star formation is defined as $\tau_{\rm SF} = \min(\tau_{\rm ff}, \tau_{\rm max})$. We follows the definition of Krumholz & Tan (2007) for the gas free-fall time,

$$\tau_{\rm ff} = \sqrt{\frac{3\pi}{32G\rho}}$$

(here ρ is the total mass density, including helium) and $\tau_{\rm max}$ is the free-fall time in the gas with $n_{\rm SF} = 50$ cm^{-3}. We adopt $\epsilon_{\rm SF} = 0.005$, which is lower than the value we adopted in Gnedin et al. (2009) and is still within the range of values advocated by Krumholz & Tan (2007). The lower value of $\epsilon_{\rm SF}$ that we adopt provides a better fit The H I Nearby Galaxy Survey (THINGS) measurements of the K-S relation (Bigiel et al. 2008).

The $\tau_{\rm sf}$ we adopt assumes that in low-density cells, in which molecular fraction $f_{\rm H_2}$ is below unity, star formation proceeds mainly in unresolved molecular clouds on subgrid scales. This assumption then also motivates setting the maximum free-fall time to $\tau_{\rm max}$ corresponding to the number density of 50 cm^{-3} typical average density of molecular clouds. The $f_{\rm H_2} < 1$ in these cells then can be viewed as reflecting the fraction of the total gas in such star-forming molecular clouds, which themselves have $f_{\rm H_2} = 1$, rather than incomplete conversion of the atomic gas into the molecular form inside the clouds.

As we show below (see Figure 8 and discussion in Section 4), the K-S relation in our simulations is not very sensitive to variations of $\epsilon_{\rm SF}$ between 0.005 and 0.01 and $n_{\rm SF}$ between 10 and 50 cm^{-3}.

3. THE ATOMIC-TO-MOLECULAR GAS TRANSITION

The effect of two primary parameters, the dust-to-gas ratio $D_{\rm MW}$ and the interstellar FUV flux $U_{\rm MW}$, on the transition from atomic-to-molecular gas is illustrated in Figure 1 as a function of the total hydrogen density, $n_{\rm H} \equiv n_{\rm H\,I} + n_{\rm H\,II} + 2n_{\rm H_2}$ (the contribution of ionized gas $n_{\rm H\,II}$ is negligible for densities shown in Figure 1). Note that in this study we do not analyze or identify individual galaxies. Instead, we select only the highest resolution cells in the refinement mesh (level 9), which are always located in the ISM of galaxies (and not, say, in the halo or intergalactic medium) in the high-resolution Lagrangian region of the simulation. Thus, only the highest resolution cells are used in Figures 1 and 3, irrespectively of which object they actually belong to.

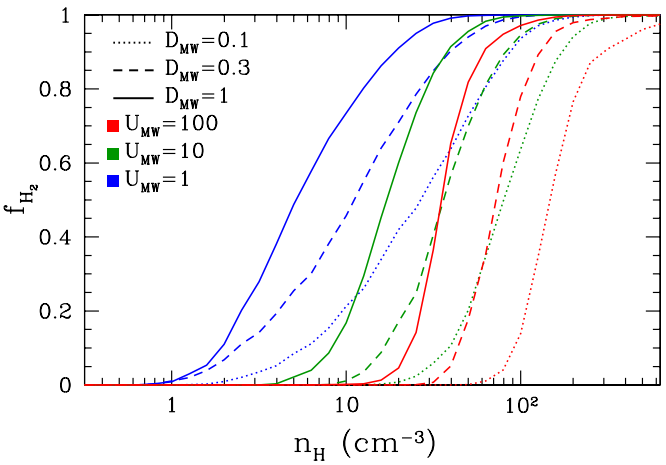

Figure 1. Average atomic-to-molecular gas transition as a function of total hydrogen number density for nine test simulations (as distinguished by colors and line styles).

(A color version of this figure is available in the online journal.)

As can be seen in the figure, both parameters affect the atomic-to-molecular transition in a non-trivial way. This scaling can be understood approximately if we ignore all physical processes except the formation of molecular hydrogen on dust and dissociation of molecular hydrogen by the UV radiation in the Lyman–Werner band. This is necessarily an approximation, as many other processes are indeed important for the detailed balance of molecular hydrogen (see the Appendix), but the formation on dust and photodissociation are the dominant processes that control the atomic-to-molecular gas transition under normal ISM conditions. In this approximation, the equilibrium abundance of molecular hydrogen can be determined from the balance of the formation and dissociation rates (cf. the Appendix):

$$n_{\rm H_2}\Gamma_{\rm LW}S_{\rm H_2}\left(N_{\rm H_2}\right)e^{-\sigma_{\rm LW}N_{\rm H}} = R_D n_{\rm H} n_{\rm H\,I}, \tag{3}$$

where $\Gamma_{\rm LW} = U_{\rm MW}\Gamma_0$ is the free space photodestruction rate and R_D and $\sigma_{\rm LW}$ are given by Equation (1). The atomic gas becomes molecular only due to self-shielding and shielding by dust (the last two factors on the left-hand side of Equation (3)). If the FUV flux is not too strong, the self-shielding by molecular hydrogen dominates; in this limit dust absorption can be neglected and Equation (3) becomes

$$\frac{f_{\rm H_2}}{1-f_{\rm H_2}} = \frac{D_{\rm MW}}{U_{\rm MW}} n_{\rm H}\frac{R_0}{\Gamma_0 S_{\rm H_2}},$$

where $f_{\rm H_2} \equiv n_{\rm H_2}/n_{\rm H}$ and we ignore ionized gas. For our ansatz for the self-shielding factor $S_{\rm H_2} \propto n_{\rm H_2}^{-3/4}$ (Equation (A11)), so

that

$$\frac{f_{\rm H_2}^{1/4}}{1-f_{\rm H_2}} \propto \frac{D_{\rm MW}}{U_{\rm MW}} n_{\rm H}^{7/4}.$$

Thus, the characteristic density at which molecular hydrogen fraction reaches a particular value (e.g., 50%) scales with the dust-to-gas ratio $D_{\rm MW}$ and the FUV radiation flux $U_{\rm MW}$ as

$$n_{\rm H} \propto \left(\frac{U_{\rm MW}}{D_{\rm MW}}\right)^{4/7}. \quad (4)$$

In the opposite regime of large $U_{\rm MW}$, the shielding by dust is expected to dominate over self-shielding, because self-shielding is a gradual function of the gas column density and may not be able to provide the required shielding for sufficiently large UV fluxes. In this regime, Equation (3) becomes

$$\frac{f_{\rm H_2}}{1-f_{\rm H_2}} = \frac{D_{\rm MW}}{U_{\rm MW}} n_{\rm H} \frac{R_0}{\Gamma_0 S_{\rm H_2}} e^{D_{\rm MW}\sigma_0 N_{\rm H}}$$

and the exponential factor is now large, so the characteristic *column* density for the atomic-to-molecular transition is

$$N_{\rm H} \propto \frac{\ln(U_{\rm MW}/D_{\rm MW})}{D_{\rm MW}}. \quad (5)$$

Thus, as Gnedin et al. (2009) mention, in the regime where dust shielding dominates, the dependence of the characteristic column density on the FUV flux $U_{\rm MW}$ is only logarithmic.

There is no way to convert between the characteristic column density and the physical gas density easily. Nevertheless, the following simple fitting formula captures the average dependence of the atomic-to-molecular transition on the dust-to-gas ratio and the FUV flux in our simulations:

$$f_{\rm H_2} \approx \frac{1}{1+\exp(-4x-3x^3)}, \quad (6)$$

where x is given by

$$x \equiv \Lambda^{3/7} \ln\left(D_{\rm MW}\frac{n_{\rm H}}{\Lambda n_*}\right). \quad (7)$$

Here $n_* = 25$ cm^{-3}, Λ is

$$\Lambda \equiv \ln\left(1 + g D_{\rm MW}^{3/7} (U_{\rm MW}/15)^{4/7}\right), \quad (8)$$

and g is a fudge factor to approximately account for the transition between the two regimes: $g \approx 1$ when self-shielding dominates and $g \propto D_{\rm MW}^{-1}$ when dust shielding dominates.

We adopt the following fitting formula for the quantity g:

$$g = \frac{1+\alpha s + s^2}{1+s},$$

where

$$s \equiv \frac{0.04}{D_* + D_{\rm MW}}, \quad \alpha = 5\frac{U_{\rm MW}/2}{1+(U_{\rm MW}/2)^2},$$

and

$$D_* = 1.5\times10^{-3} \times \ln(1+(3U_{\rm MW})^{1.7})$$

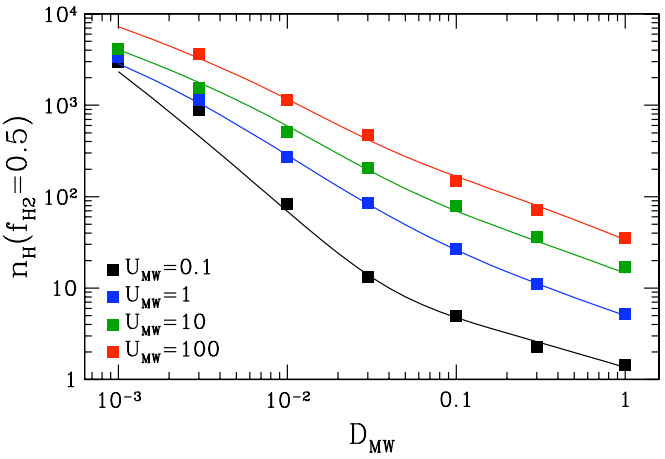

Figure 2. Average total hydrogen number density of atomic-to-molecular gas transition (defined as $f_{\rm H_2} = 0.5$) as a function of the scaled dust-to-gas ratio $D_{\rm MW}$ and the FUV flux $U_{\rm MW}$ for all our test simulations. The point ($D_{\rm MW} = 0.001, U_{\rm MW} = 100$) is missing because the resolution of our simulations is insufficient to capture the atomic-to-molecular transition in such extreme conditions. Solid lines show fitting formula of Equation (9).

(A color version of this figure is available in the online journal.)

describes the transition to the regime when the formation of H_2 via the gas-phase reactions dominates.

Figure 2 shows the value of the total (molecular, atomic, and ionized—although the contribution of ionized gas in all equations in this section is completely negligible) hydrogen density at which molecular fraction reaches $f_{\rm H_2} = 0.5$ ($x = 0$). Our fitting formulae give the following approximate expression for this density:

$$n_{\rm H\,I\to H_2} \equiv n_{\rm H}(f_{\rm H_2} = 0.5) \approx n_* \frac{\Lambda}{D_{\rm MW}}. \quad (9)$$

This equation is a better approximation than the simple step-function ansatz proposed in Gnedin et al. (2009). Figure 2 demonstrates that Equation (9) indeed provides an accurate model for the dependence of $n_{\rm H}(f_{\rm H_2} = 0.5)$ on $D_{\rm MW}$ and $U_{\rm MW}$.

Figure 3 shows that Equation (6) works well for $f_{\rm H_2} \gtrsim 0.1$ for all simulated cases (four values of $U_{\rm MW}$ and seven values of $D_{\rm MW}$), but it becomes somewhat less accurate for lower molecular fractions. The accuracy in the low $f_{\rm H_2}$ regime can be improved with a simple modification: replacing x in Equation (6) with $x/g^{1/4}$. This change provides a more accurate fit for the range $10^{-5} \lesssim f_{\rm H_2} \lesssim 0.1$, but is less accurate than the above approximation for $f_{\rm H_2} > 0.1$. Given that for modeling star formation the range $f_{\rm H_2} \gtrsim 0.1$ is most relevant, we use the unmodified form of our fit as the fiducial approximation.

Neither form of this fit describes the equilibrium H_2 abundance ($f_{\rm H_2} \sim 10^{-6}$–10^{-8}) in the warm ISM. Such a small abundance is, of course, not relevant to star formation.

4. THE KENNICUTT–SCHMIDT RELATION AND ITS DEPENDENCE ON THE DUST-TO-GAS RATIO AND THE FUV FLUX

The physics of the transition from atomic-to-molecular phase, discussed in the previous section, controls which local regions within the ISM of simulated galaxies have high-molecular fraction and, hence, become the sites of star formation. Although the local rate of star formation in these regions is sensitive to the

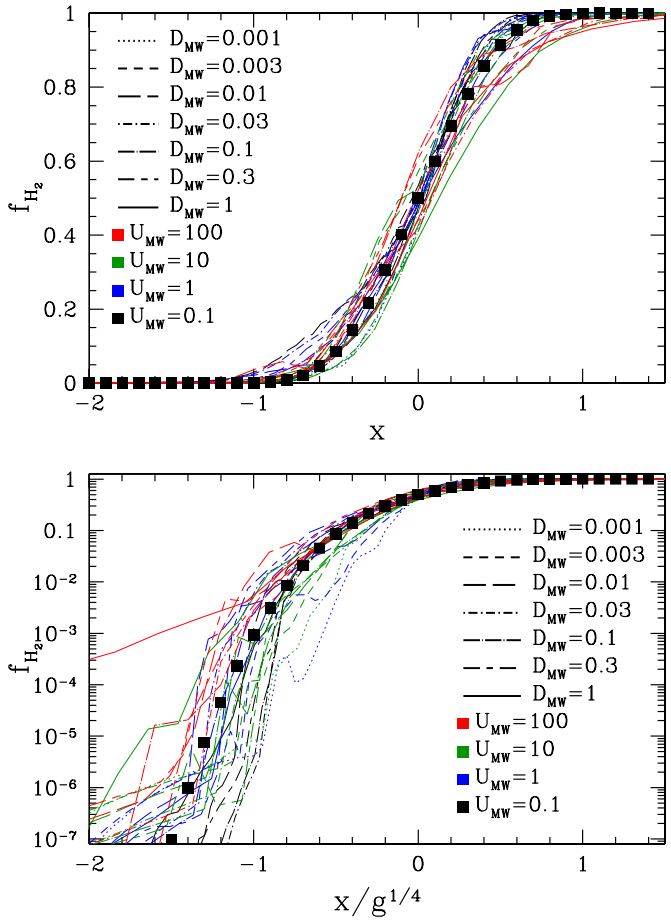

Figure 3. Average atomic-to-molecular gas transition as a function of the factorized variable x (Equation (7)) for all our test simulations (as distinguished by colors and line styles). The top panel shows the linear scaling of the y-axis (most relevant for modeling star formation) while the bottom panel shows the y-axis in log. Black squares show the approximation from Equation (6).

(A color version of this figure is available in the online journal.)

parameters of the H_2 formation model and star formation recipe, the global SFR surface density on larger, kiloparsec scales depends on the density and UV flux distribution within larger scales that are modeled self-consistently in the simulations. Therefore, once we fix the parameters of the model controlling the chemistry and star formation on small scales, we can examine the *predicted* K-S relation between the surface densities of various gas phases and the surface density of star formation averaged on large scale.

Observationally, only the surface densities of atomic and molecular gas are directly measured and included in the estimate of the "total" surface gas density, $\Sigma_{\rm H}$. However, as we demonstrate below, the ionized gas may contribute significantly to the total gas surface density under some conditions. Therefore, we deliberately avoid using the ambiguous notation $\Sigma_{\rm H}$ and instead use the following notation explicitly indicating the components that are included in the surface density:

$$\Sigma_{\rm H\,I+H\,II+H_2} \equiv \Sigma_{\rm H\,II} + \Sigma_{\rm H\,I} + \Sigma_{\rm H_2},$$

for the total surface density, including both neutral and ionized gas, and

$$\Sigma_{\rm H\,I+H_2} \equiv \Sigma_{\rm H\,I} + \Sigma_{\rm H_2},$$

for the surface density, including only neutral atomic and molecular gas. Note that we follow the observational practice and do not include the contribution of helium in the above gas surface densities. We emphasize again that in observational work the total gas density is commonly identified with this second quantity, $\Sigma_{\rm H} = \Sigma_{\rm H\,I+H_2}$.

As we mentioned in the previous section, this distinction is unnecessary for studying the atomic-to-molecular gas transition on small scales, because the fraction of ionized gas is always small at densities at which the molecular fraction is significant. In other words, high-f_{H_2} regions are always surrounded by neutral atomic envelopes containing little ionized gas. However, regions of a kiloparsec scale can contain a mix of different ISM phases: from low-density ionized gas to high-density, molecular regions. In fact, diffuse ionized ISM gas is ubiquitous in nearby galaxies (e.g., Hoopes & Walterbos 2003). The warm ($\sim 10^4$ K) diffuse ionized gas is present both inside the disk and at large distances (up to ~2–4 kpc) from the midplane both in the MW (Reynolds 1989, 1991; Gaensler et al. 2008) and in other nearby galaxies (e.g., Hoopes et al. 1999; Collins et al. 2000; Rossa & Dettmar 2003; see Haffner et al.; 2009 for review). This ionized gas can be a significant fraction of the total gas density. In the MW, for example, the warm ionized gas accounts for ~25% of the total hydrogen column density of the disk (Reynolds 1991; Haffner et al. 2009). One has to keep in mind the possible presence of such gas in theoretical interpretations of the K-S relation.

For comparison with observations, the SFR in the simulations is averaged over 20 Myr and the gas and SFR surface densities are averaged on the scale of 500 pc. This specific choice is similar to the averaging spatial scale and star formation indicator used in the THINGS measurements (Salim et al. 2007; Bigiel et al. 2008). We tested the sensitivity of the predicted K-S relation to the specific choice of the averaging temporal and spatial scales; such a comparison is presented in the Appendix (see Figure 14). Overall, the K-S relation is robust to changes of spatial and temporal averaging scales with the range 0.5–2.0 kpc and 20–100 Myr, respectively. Some modest trends are observed, but these are in general agreement with observations.

We compute the surface densities averaged over 500 pc scale by identifying cells in the adaptive mesh refinement hierarchy that are close to this scale, and using density in such cells, ρ, to compute surface densities as $\Sigma = \rho\Delta x$, where Δx is the size of the cells. Although this is an approximate calculation of the surface density, it is not very far from the exact calculation, because the scale of 500 pc is close to the thickness of the typical disks in the simulations. This is approximately analogous to the observational studies, which typically correct the observed surface densities for the inclination angle.

In the rest of this section, we use all 500 pc cells in the computational domain. However, since we only use cells with non-zero SFR, and, by construction, star formation in our simulations only occurs in the molecular gas (Equation (2)), only 500 pc cells that contain sections of galactic disks are shown in the subsequent figures.

In Figure 4, we show the *average* relation between $\Sigma_{\rm SFR}$ and the *total* surface density of gas (atomic, molecular, and ionized), $\Sigma_{\rm H\,I+H\,II+H_2}$, for nine different representative combinations of dust-to-gas ratio and the interstellar FUV flux $D_{\rm MW}$ and $U_{\rm MW}$. We chose to average the surface density of gas in bins of $\Sigma_{\rm SFR}$ (so that the $\Sigma_{\rm SFR}$–$\Sigma_{\rm H\,I}$ relation can be traced reliably), and we verified that averaging $\Sigma_{\rm SFR}$ in bins of $\Sigma_{\rm H\,I+H\,II+H_2}$ leads to similar results.

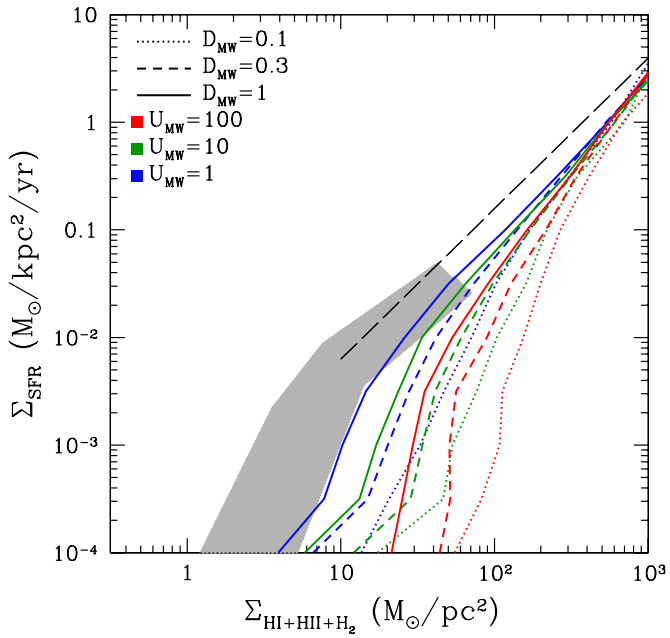

Figure 4. Average relation between $\Sigma_{\rm SFR}$ and the *total* surface density of gas (atomic, molecular, and ionized) for nine different representative combinations of dust-to-gas ratio and the interstellar FUV flux (colored lines). The long-dashed line is the best-fit relation of Kennicutt (1998) for $z \approx 0$ galaxies. The gray shaded area shows the K-S relation for the local dwarf and normal spiral galaxies measured by the THINGS project (Bigiel et al. 2008).

(A color version of this figure is available in the online journal.)

As could be expected, both the dust-to-gas ratio $D_{\rm MW}$ and the UV flux $U_{\rm MW}$ affect the relation significantly by affecting the atomic-to-molecular transition and the fraction of neutral gas in the ISM patches. Notably, the predicted $\Sigma_{\rm SFR}$–$\Sigma_{\rm H\,I+H\,II+H_2}$ relation does not agree with observations for any combination of $U_{\rm MW}$ and $D_{\rm MW}$.

However, as we emphasized above, observational measurements often do not account for the contribution of ionized gas to the surface density. We therefore present a separate prediction for the K-S relation for the neutral gas only in Figure 5 for a representative subset of our test simulations. This figure demonstrates that the predicted $\Sigma_{\rm SFR}$–$\Sigma_{\rm H\,I+H_2}$ relation for the parameter values representative of local galaxies ($D_{\rm MW} \sim 1$ and any value of $U_{\rm MW}$) is in good agreement with both the older measurement of Kennicutt (1998) and with the recent measurements by THINGS (Bigiel et al. 2008). In particular, our model approximately reproduces the rapid decrease of the SFR and increase of the scatter at $\Sigma_{\rm H\,I+H_2} < 10\,M_\odot$ pc^{-2} and the change in the slope of the SFR versus gas surface density from $\Sigma_{\rm SFR} \propto \Sigma^{1.0}_{\rm H\,I+H_2}$ to $\Sigma_{\rm SFR} \propto \Sigma^{1.4}_{\rm H\,I+H_2}$ at $\Sigma_{\rm H\,I+H_2} \approx 10^2\,M_\odot$ pc^{-2}. The model also reproduces the observed scatter of the K-S relation reasonably well (we explore the scatter in this relation as a function of metallicity, UV flux, and scale in a separate study; Feldmann et al. 2010).

A qualitatively similar trend of the K-S relation with metallicity was recently predicted by Krumholz et al. (2009c) using a model of atomic-to-molecular transition in molecular complexes based on the Wolfire et al. (2003) semi-analytic model of atomic ISM (see also McKee & Krumholz 2010). Their model predicts significant steepening of the K-S relation below gas surface density of $\Sigma_{\rm H} \lesssim 10/cZ\,M_\odot$ pc^{-2}, where Z is the metallicity of the gas in the units of $Z_\odot$ and c is the ISM clumping factor. The latter reflects the difference between the surface density of the ISM averaged on some scale >100 pc and the surface density of individual giant molecular complexes on the scale of 100 pc. For averaging scales of 500 pc used in our calculations, the clumping factor should be $c \sim 2$–5 (Krumholz et al. 2009c). The model thus predicts the steepening of the K-S relation at surface

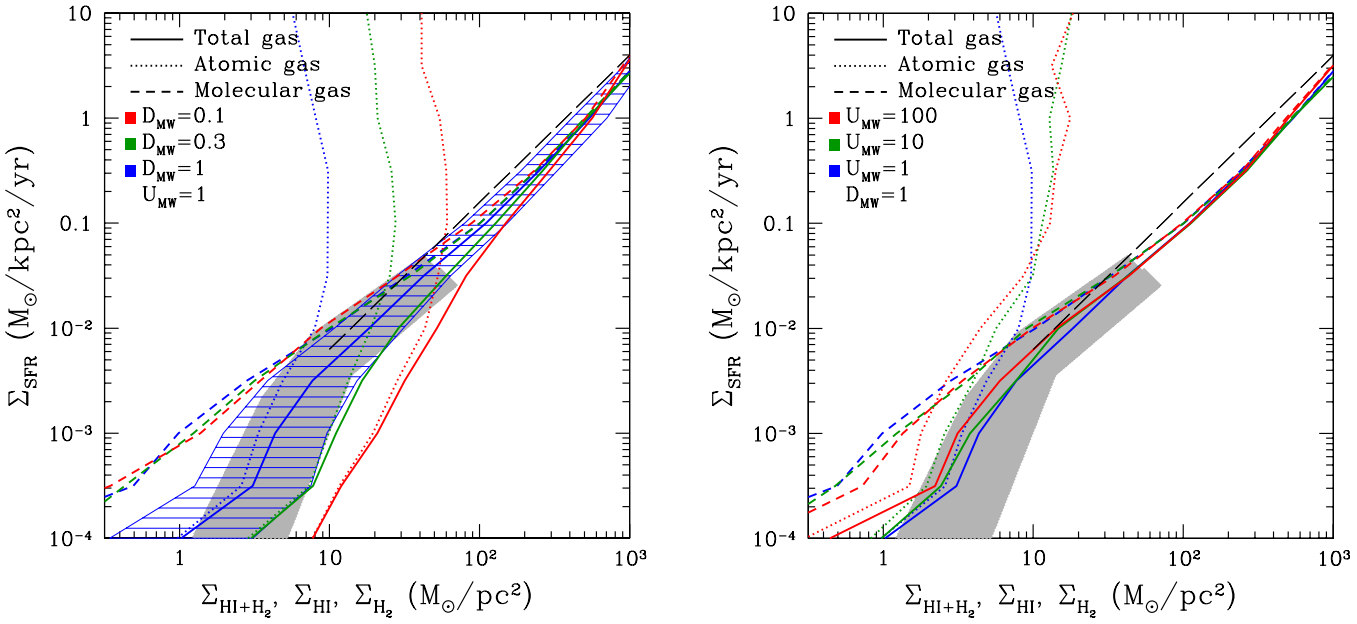

Figure 5. Average K-S relations for the *neutral* gas (atomic and molecular) predicted in models with different representative values for the dust-to-gas ratio (left panel) and the interstellar FUV radiation flux (right panel) are shown as colored lines. Dotted, short-dashed, and solid lines show the relation between $\Sigma_{\rm SFR}$ and $\Sigma_{\rm H_1}$, $\Sigma_{\rm H_2}$, and $\Sigma_{\rm H\,I+H_2}$ individually. The shaded blue band on the left panel shows the rms scatter for the $D_{\rm MW} = U_{\rm MW} = 1$ model. The observed relations (long-dashed line and gray band) are the same as in Figure 4.

(A color version of this figure is available in the online journal.)

density values that are considerably lower than the transition surface density of $\Sigma_{\rm H} \approx 50$–$100\,M_\odot\,{\rm pc}^{-2}$ for low metallicity seen in Figure 5. Thus, their results are consistent with ours for the lowest values of the clumping factors ($\sim$2) in their plausible range of values.

The K-S relations shown in Figures 4 and 5 can be accurately described by a simple fitting formula. Since stars only form in molecular gas, the SFR surface density is proportional to the surface density of molecular gas,

$$\Sigma_{\rm SFR} = \frac{1}{\tau_{\rm SF}}\Sigma_{\rm H_2},$$

where $\tau_{\rm SF}$ is the timescale for star formation (that may itself depend on the molecular gas surface density). If the neutral gas surface density $\Sigma_{\rm H\,I+H_2}$ is used as an argument, the reduced SFR at low gas surface density needs to be taken into account,

$$\Sigma_{\rm SFR} = \frac{1}{\tau_{\rm SF}}\frac{\Sigma_{\rm H\,I+H_2}}{(1+\Sigma_c/\Sigma_{\rm H\,I+H_2})^2}, \qquad (10)$$

where Σ_c is the characteristic surface density of neutral gas at which the relation steepens. At large gas surface densities (i.e., $\Sigma_c \ll \Sigma_{\rm H\,I+H_2}$) we have

$$\Sigma_{\rm SFR} \approx \frac{1}{\tau_{\rm SF}}\left(\Sigma_{\rm H\,I+H_2} - \Sigma_{\rm H\,I}^{\infty}\right), \qquad (11)$$

where $\Sigma_{\rm H\,I}^{\infty}$ is the saturation value of H I surface density, i.e., the maximum $\Sigma_{\rm H\,I}$ reached by gas as its total surface density increases to large values. Note that comparison of this equation with the formula of Equation (10) shows that

$$\Sigma_c = \frac{\Sigma_{\rm H\,I}^{\infty}}{2}.$$

Figure 5 demonstrates that, while the dust-to-gas ratio $D_{\rm MW}$ plays the dominant role in controlling the turnover in the $\Sigma_{\rm SFR}$–$\Sigma_{\rm H\,I+H_2}$ relation at low surface densities for $D_{\rm MW} \gtrsim 0.1$, this is no longer the case at lower dust-to-gas ratios. Figure 6 shows the dependence of the characteristic "threshold" surface density Σ_c on $U_{\rm MW}$ and $D_{\rm MW}$ for the full suite of our models. At $D_{\rm MW} \lesssim 0.1$, Σ_c changes by an order of magnitude for $U_{\rm MW}$ changing by three orders of magnitude between 0.1 and 100. Thus, although the dependence of the K-S relation on the FUV flux for higher dust content systems is expected to be weak, it can be stronger for dwarf galaxies at $z \approx 0$ and in high-z galaxies with low dust-to-gas ratios.

The dependence of the H I saturation surface density on our two main parameters can be understood qualitatively if we assume that the density distribution in the ISM is approximately self-similar. Let us consider a large-scale region over which we measure the total hydrogen surface density $\Sigma_{\rm H\,I+H\,II+H_2}$. Within this region the total hydrogen density has some density probability function (defined as a fraction of surface density contributed by the gas with the density between $n_{\rm H}$ and $n_{\rm H} + dn_{\rm H}$), which in general depends on $\Sigma_{\rm H\,I+H\,II+H_2}$,

$$d\Sigma_{\rm H\,I+H\,II+H_2} = \phi(n_{\rm H}, \Sigma_{\rm H\,I+H\,II+H_2})dn_{\rm H}.$$

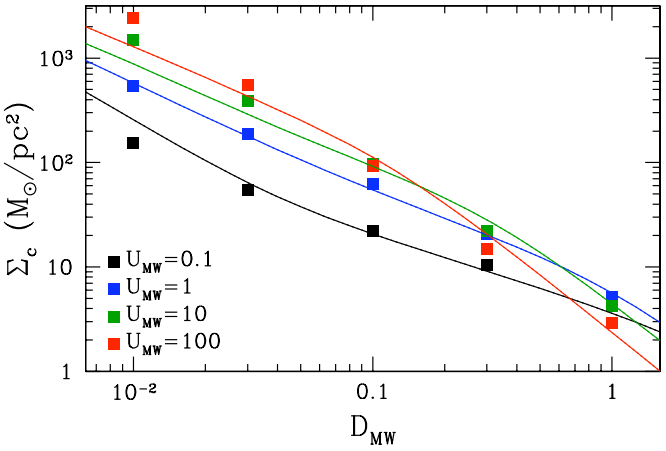

Figure 6. Characteristic threshold surface density Σ_c as a function of two main parameters $D_{\rm MW}$ and $U_{\rm MW}$ for all our test simulations. Cases with $D_{\rm MW} < 0.01$ are not shown, as in our simulations gas at such low values of the dust-to-gas ratio never becomes fully molecular on 500 pc scale (and, thus, $\tilde{\Sigma}_{\rm SFR}$ cannot be determined). The solid lines show the fitting formula of Equation (14).
(A color version of this figure is available in the online journal.)

If the density distribution is approximately self-similar, a region with a higher surface density will have more dense gas, i.e.,

$$\phi(n_{\rm H}, \Sigma_{\rm H\,I+H\,II+H_2}) = \psi(\xi),$$

where $\xi = n_{\rm H}/\Sigma_{\rm H\,I+H\,II+H_2}$ and

$$\int_0^\infty \psi(\xi)d\xi = 1.$$

The atomic hydrogen surface density is then simply

$$\Sigma_{\rm H\,I} = \int_0^\infty f_{\rm H\,I}\phi dn_{\rm H} = \Sigma_{\rm H\,I+H\,II+H_2}\int_0^\infty f_{\rm H\,I}\psi(\xi)d\xi.$$

If we assume that most of the atomic hydrogen mass is at densities near the atomic-to-molecular transition density $n_{\rm H\,I\to H_2}$ (which is the case in our simulations), then we can use our parameterization from Equation (6) a function of factorized variable x (Equation (7)), so that

$$d\xi = \frac{n_{\rm H}}{\Sigma_{\rm H\,I+H\,II+H_2}}\frac{dx}{\Lambda^{3/7}},$$

and

$$\Sigma_{\rm H\,I} = \frac{1}{\Lambda^{3/7}}\int_{-\infty}^{\infty} f_{\rm H\,I}n_{\rm H}\psi(\xi)dx.$$

The last integral cannot be taken exactly, but given that the atomic-to-molecular transition is a rather steep function of the gas density, the integral can be approximated as

$$\Sigma_{\rm H\,I} \approx \frac{1}{\Lambda^{3/7}}\left(f_{\rm H\,I}n_{\rm H}\psi\right)|_{\rm H\,I\to H_2}\Delta x = \frac{1}{\Lambda^{3/7}}\frac{1}{2}n_{\rm H\,I\to H_2}\psi(\xi_{\rm H\,I\to H_2}/2)\Delta x, \qquad (12)$$

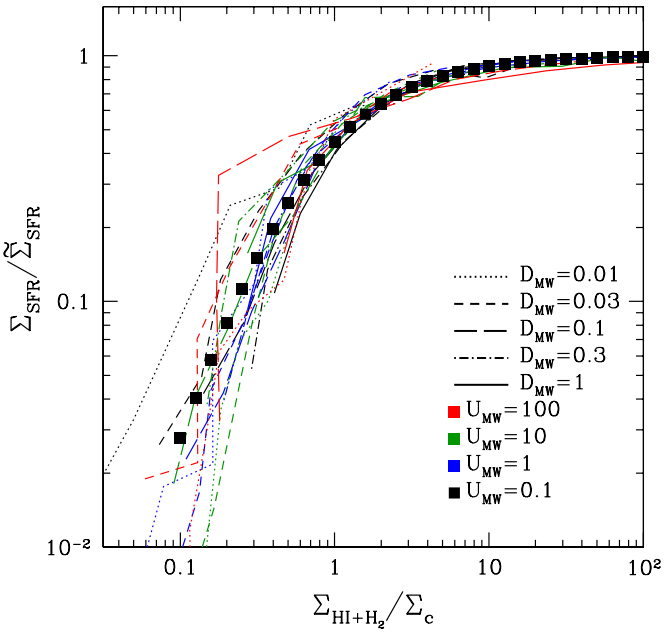

Figure 7. Scaled K-S relation as a function of the neutral gas surface density, scaled by the characteristic surface density Σ_c. Black squares show the fitting formulae (10) with Σ_c given by Equation (14) and $\tilde{\Sigma}_{SFR}$ measured directly from the simulation as the SFR density in the molecular gas. Cases with $D_{MW} < 0.01$ are not shown, as in our simulations gas at such low values of the dust-to-gas ratio never becomes fully molecular on 500 pc scale (and, thus, $\tilde{\Sigma}_{SFR}$ cannot be measured).

(A color version of this figure is available in the online journal.)

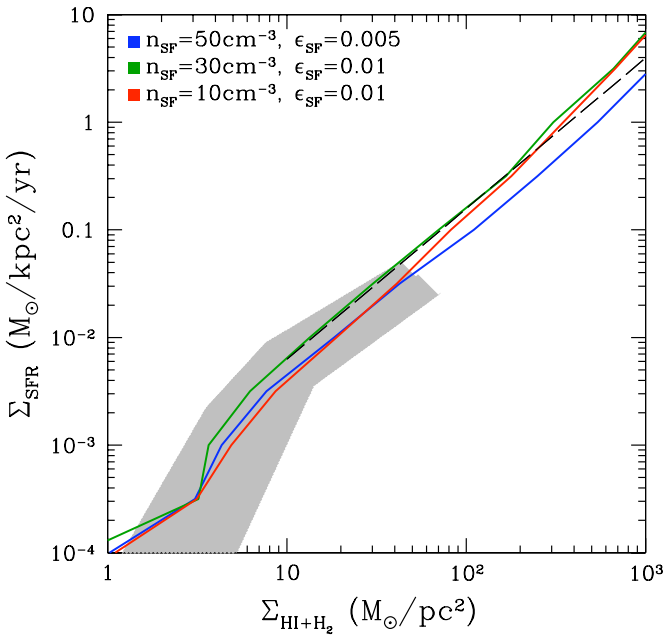

Figure 8. Dependence of the K-S relation for the neutral gas (atomic and molecular) on the parameters of the star formation recipe (2). The long-dashed line is the best-fit relation of Kennicutt (1998) for $z \approx 0$ galaxies. The gray shaded area shows the K-S relation for the local dwarf and normal spiral galaxies measured by the THINGS project (Bigiel et al. 2008).

(A color version of this figure is available in the online journal.)

where $\Delta x \sim 1$ is the width of the atomic-to-molecular transition ($f_{H\,I} = f_{H_2} = 0.5$) in the variable x, which should be essentially independent of any physical parameter.

The saturation H I surface density $\Sigma^{\infty}_{H\,I}$ is obtained from Equation (12) in the limit of $\Sigma_{H\,I+H\,II+H_2} \to \infty$, in which case the argument of ψ in Equation (12) can be replaced with zero, and we finally obtain[5]

$$\Sigma^{\infty}_{H\,I} \approx \psi(0)\frac{n_{H\,I\to H_2}}{2\Lambda^{3/7}}\Delta x \propto \frac{\Lambda^{4/7}}{D_{MW}}. \qquad (13)$$

We find that this scaling works well in our simulations, except in the limit of large D_{MW} and large U_{MW}, when the density of the ionized-to-atomic transition is not negligible compared to the density of the atomic-to-molecular transition. As a consequence, the contribution of the ionized gas is not negligible compared to the atomic gas, which leads to a decrease of $\Sigma^{\infty}_{H\,I}$ compared to the value predicted by Equation (13). In the extreme case, we consider ($D_{MW} = 1$, $U_{MW} = 100$) the saturation H II surface density is 3–4 times higher than the saturation H I surface density.

The following simple fitting formula corrects for this deficiency and provides a good fit for the characteristic "threshold" surface density, Σ_c, in all test cases we consider,

$$\Sigma_c = 20\,M_\odot\ \mathrm{pc}^{-2}\frac{\Lambda^{4/7}}{D_{MW}}\frac{1}{\sqrt{1+U_{MW}D^2_{MW}}}. \qquad (14)$$

The accuracy of this fitting formula is demonstrated in Figures 6 and 7. For very low values of $D_{MW} \lesssim 0.01$, the fit is not very accurate. This is most likely due to the limited volume of our simulations: at such low dust-to-gas ratios the atomic-to-molecular transition shifts to extremely high gas densities, $n_H \sim 10^3\,\mathrm{cm}^{-3}$, and our simulations lack 500 pc sized regions that would be dominated by such dense gas. Large volume simulations containing substantially more massive galaxies will be needed to test the accuracy of the fitting formula (14) in this regime.

Finally, we have checked that our results are not particularly sensitive to the specific choice of the fiducial parameters ϵ_{SF} and n_{SF}. While the fiducial values provide the best fit to the median values of THINGS measurements (Bigiel et al. 2008), a substantial variation in the adopted values for these parameters has only mild effect on our results, as we demonstrate in Figure 8.

5. STAR FORMATION RECIPES

5.1. Recipe for Galaxy Formation Simulations

In Section 3, we have shown that atomic-to-molecular transition density can be well fit by fitting functions as a function of dust-to-gas ratio and FUV flux (e.g., Equation (6)). These fitting functions are an approximation to the *average* dependence of the molecular fraction on the total hydrogen density. The scatter in this relation around the mean may be important for particular observational measurements of the molecular abundance in the ISM. However, it is interesting to ask the question

[5] Note, that, for a general self-similar distribution, the contribution to the surface density $\Delta\Sigma_l$ from the lowest density gas with $n < n_l$ is expected to be linear on the gas density limit n_l, $\Delta\Sigma_l \propto n_l$ (since there are no small characteristic density values to provide scaling for a non-trivial density dependence). Since

$$\Delta\Sigma_l = \Sigma_{H\,I+H\,II+H_2}\int_0^{\xi_l}\psi(\xi)d\xi \approx \Sigma_{H\,I+H\,II+H_2}\psi(0)\xi_l = \psi(0)n_l,$$

generically $\psi(0)$ should be non-zero.

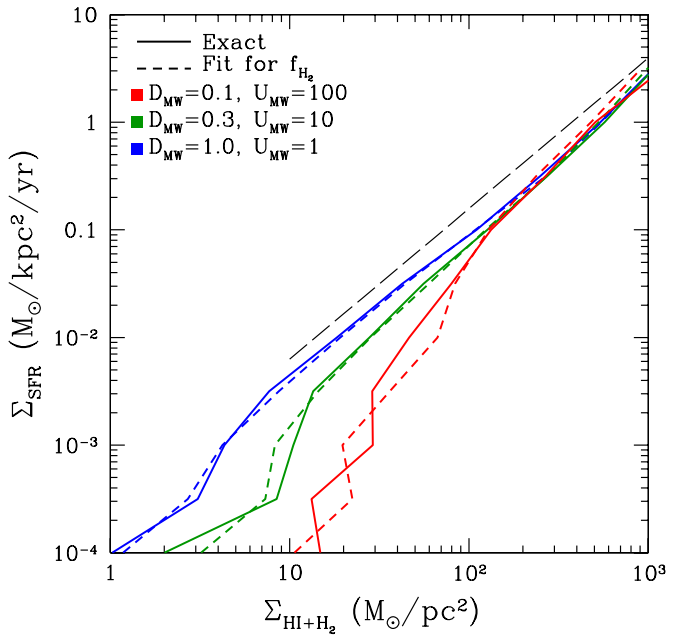

Figure 9. Comparison of the K-S relation for the neutral gas (atomic and molecular) for the full simulations and test runs which used Equation (6) to estimate the molecular fraction in the gas for a representative subset of values for D_{MW} and U_{MW}.

(A color version of this figure is available in the online journal.)

of whether we can reproduce results of our full simulations by using the fit for molecular fraction given by Equation (6) in star formation recipe of Equation (2), instead of the true f_{H_2} calculated using our full chemistry model. The results of such tests are shown in Figure 9, which demonstrates that using the fit to $f_{H_2}(n_H)$ gives results closely matching results of the full calculations.

This means that the approximation of Equation (6) can be used to implement the H_2-based star formation recipe in galaxy formation simulations that do not follow the full molecular chemistry, provided that the resolution of the simulations is sufficiently high ($\sim$100 pc) and that the values for the parameters D_{MW} and U_{MW} could be estimated or assumed. The dust-to-gas ratio D_{MW} can be estimated using local gas metallicity Z. Although the observed relation between D_{MW} and Z has a substantial scatter, on average the dust-to-gas ratio appears to be directly proportional to the gas metallicity,

$$D_{MW} = \frac{Z}{Z_\odot},$$

both for normal galaxies (Inoue 2003; Draine et al. 2007; Calura et al. 2008) and in low-metallicity dwarfs (Lisenfeld & Ferrara 1998; Hirashita 1999; Calura et al. 2008; Madden 2008). Such a simple relation is, necessarily, a crude approximation, since not only the abundance, but even the properties of dust are known to be different in different galaxies.

Relating the local FUV flux U_{MW} is trickier, but sensible estimates can be made using the local SFR rate averaged on a certain scale, as was done, for example, by Robertson & Kravtsov (2008). Given the steepness of the atomic-to-molecular transition, the H_2-based star formation recipe amounts to the metallicity and FUV flux-dependent density threshold for star formation.

5.2. Star Formation Recipe for Semi-analytic Models

The dependence of the K-S relation on the dust-to-gas ratio and the FUV flux in our test simulations described in Section 4 can also be encapsulated by a simple recipe. Such a recipe can be used in semi-analytic models, in which the radial dependence of gas surface density, star formation, and chemical enrichment is modeled explicitly (e.g., Firmani & Avila-Reese 2000; Kravtsov et al. 2004; Dutton et al. 2007).

As we discussed above, the dependence of the K-S relation on D_{MW} and U_{MW} in our models is due to the dependence of the characteristic H I surface density, Σ_c, on these variables. We therefore parameterize the K-S relation by the following fitting formula,

$$\Sigma_{SFR} = \frac{\tilde{\Sigma}_{SFR}(\Sigma_{H\,I+H_2})}{(1+\Sigma_c/\Sigma_{H\,I+H_2})^2}, \quad (15)$$

where Σ_c is given by Equation (14) and $\tilde{\Sigma}_{SFR}(\Sigma_{H\,I+H_2})$ is the SFR in the fully molecular gas at this surface density. For the latter, one can adopt either the original Kennicutt fit (Kennicutt 1998),

$$\tilde{\Sigma}_{SFR,K} = 2.4\times10^{-4}\frac{M_\odot}{\mathrm{kpc}^2\ \mathrm{yr}}\left(\frac{\Sigma_{H\,I+H_2}}{1\,M_\odot\ \mathrm{pc}^{-2}}\right)^{1.4}, \quad (16)$$

or the fit to the data presented in Bigiel et al. (2008), similar to the one proposed in Krumholz et al. (2009b),

$$\tilde{\Sigma}_{SFR,B} = \frac{\Sigma_{H\,I+H_2}}{800\ \mathrm{Myr}}\max\left(1, \frac{\Sigma_{H\,I+H_2}}{\Sigma_h}\right)^{\beta_h-1}, \quad (17)$$

with the values of $\Sigma_h \approx 200\,M_\odot$ pc^{-2} and $\beta_h \approx 1.5$. Note that neither the slope at high surface densities β_h nor the characteristic surface density Σ_h at which the slope steepens are well constrained by the current observations.

Figure 7 shows that the fitting formula for the K-S relation of Equation (15) together with Equation (14) reproduces the dependence of the K-S relation on U_{MW} and D_{MW} in simulations remarkably well. In semi-analytic models, this formula can be used if one has some prescription for estimating D_{MW} and U_{MW} in model galaxies. As we noted in the previous sections, these variables can be estimated approximately from the local metallicity of the gas and local SFR.

6. DISCUSSION AND CONCLUSIONS

We have presented results of a phenomenological model for the formation of molecular hydrogen and have illustrated the dependence of molecular fraction on the gas density, dust-to-gas ratio, and far UV radiation flux. We have also presented the large-scale K-S relation arising in our simulated galaxies when the local star formation is based on the density of molecular (rather than total) gas. Such an approach allows us to avoid arbitrary density and temperature thresholds typically used in star formation recipes. Our results show that both the molecular fraction and the K-S relation are sensitive to the dust-to-gas ratio and the FUV flux, although the sensitivity of the K-S relation to the dust-to-gas ratio is stronger than the sensitivity to the FUV flux.

We parameterize the dependences observed in our simulations by fitting formulae (Sections 3 and 4), which can be used to approximately account for H_2 formation and H_2-based star formation in simulations, which do not include a full H_2 formation model and RT (see Section 5.1). We demonstrate that our fitting formulae, when applied to realistic simulations, produce results that are close to those obtained in simulations with the full H_2 formation model and RT (Figure 9).

We also provide fitting formulae for the dust-to-gas and the FUV radiation flux dependence of the K-S relation that can be used in the semi-analytic models of galaxy formation (Section 5.2). One recent example of a model where such dependences can be relevant is the study of Dutton et al. (2010). The results of that study indicate that the redshift evolution of SFR–M_* relation of galaxies depends on the evolution of the relation between stellar and molecular masses. Dutton et al. (2010) find that, in their model, the effective surface density of atomic hydrogen is $\Sigma_{\rm H\,I} \approx 10\,M_\odot\,{\rm yr}^{-1}$ and does not evolve with redshift. Our results, however, indicate that $\Sigma_{\rm H\,I}$ should increase with increasing redshift, as metallicities (and, hence, the dust abundance) of galaxies decrease and their FUV fluxes increase. Conversely, the M_*–$M_{\rm H_2}$ and SFR–M_* relations should evolve differently if their expected dependence on the dust-to-gas ratio and the FUV flux is taken into account. Given that at lower metallicities (and, hence, the dust abundance) we expect a smaller SFR for the same amount and spatial distribution of neutral gas, the trends described in this paper may potentially explain why the model of Dutton et al. (2010) overpredicts the specific star formation rate (SSFR $\equiv$ SFR/M_*) of small-mass galaxies at $z \gtrsim 3$.

One of the most interesting results of our simulations is that significant amounts of ionized gas can be present around high-redshift gaseous disks. This ionized gas is akin to the diffuse ionized gas observed in local galaxies (e.g., Hoopes & Walterbos 2003; Haffner et al. 2009) and the MW (Reynolds 1989, 1991; Gaensler et al. 2008). Our results indicate that the ionized gas may dominate the gas mass at low surface densities ($\Sigma \lesssim 10\,M_\odot\,{\rm yr}^{-1}$). Furthermore, our simulations show that ionized gas can remain a significant mass component at higher gas surface densities in environments with low dust content and/or high FUV fluxes (e.g., compare gas surface densities for a given $\Sigma_{\rm SFR}$ in Figures 4 and 5). One has to keep in mind the possible presence of significant amounts of ionized gas in theoretical interpretations of the K-S relation and observational estimates of the total gas mass. The significantly different K-S relation in the low dust-to-gas ratio, high FUV flux environments of high-redshift galaxies may also strongly bias gas mass estimates that use $z = 0$ calibration of that relation (e.g., Erb et al. 2006; Mannucci et al. 2009).

As we discussed in Gnedin & Kravtsov (2010), the dust-to-gas ratio and the FUV flux dependence of the K-S relation that we observe in our simulations has a number of important implications for galaxy evolution, such as a lower efficiency of star formation in damped Lyman-alpha systems, star formation confined to the highest gas surface densities of high-z disks, and generally longer gas consumption timescales in gaseous disks of high-redshift galaxies. The latter can be, at least partly, responsible for the prevalence of disk-dominated galaxies at low redshifts. This is because a low efficiency of star formation can maintain disks gas-rich until major mergers become rare. The outer, mostly *gaseous* regions of high-redshift disks should be more resistant against dynamical heating in mergers (e.g., Robertson et al. 2004, 2006; Springel & Hernquist 2005) and would help maintain forming stellar disks dynamically cold during minor mergers (Moster et al. 2010) at later epochs. Moreover, minor mergers of forming disks should be largely gaseous, and gas brought in by such mergers should be deposited at large radii as it is ram pressure stripped by interaction with the gaseous disk and/or halo around it. This should prevent the formation of large bulges, which was plaguing galaxy formation models, and instead lead to the formation of more extended, higher angular momentum disks. This scenario is borne out in recent galaxy formation simulations of Agertz et al. (2011), who show that a low efficiency of star formation at high redshifts leads to more realistic disks and smaller bulge-to-disk ratios.

Another interesting consequence of the complex dependence of the K-S relation on the dust-to-gas ratio and the FUV flux may be relevant to our own backyard. Recently, Orban et al. (2008) noted that star formation histories of MW satellites can only be explained by a K-S relation (Equation (16)) with the sharp threshold if the threshold varies semi-randomly within a modest dispersion of about 0.1 dex. This variation is consistent with the variation given by Equation (14) for the values of $D_{\rm MW}$ and $U_{\rm MW}$ typical for dwarf galaxies ($D_{\rm MW} \gtrsim 0.1$, $U_{\rm MW} \gtrsim 1$). Since star formation histories of galactic satellites are known to be highly variable (Mateo 1998; Dolphin et al. 2005), the FUV flux is expected to vary accordingly; such variations may be responsible for the needed variation of the threshold in the K-S relation, or, more precisely, the characteristic surface density Σ_c from Equation (14).

The high mass-to-light ratios (and hence low star formation efficiencies) of the Local Group dwarf spheroidal galaxies may also be partially explained by the environmental dependence of H_2 abundance and, hence, star formation. Star formation in such low metallicity, low dust content dwarf galaxies should be confined only to the highest gas surface densities (i.e., the central regions) while leaving the bulk of the gas at lower gas surface densities inert to star formation. This is consistent with observations of local dwarf low surface brightness galaxies, which exhibit very low molecular gas fractions and anemic SFRs (Matthews et al. 2005; Das et al. 2006; Boissier et al. 2008; Wyder et al. 2009; Roychowdhury et al. 2009).

The examples described above illustrate the importance of further investigation of the effects of environmental dependences of the K-S relation discussed in this paper. The results and fitting formulae that we present should aid in implementing such dependences in both cosmological simulations and semi-analytic models and should thus help to explore a wide range of possible effects.

This work was supported in part by the DOE at Fermilab, by the NSF grants AST-0507596 and AST-0708154, and by the Kavli Institute for Cosmological Physics at the University of Chicago through the NSF grant PHY-0551142 and an endowment from the Kavli Foundation. The simulations used in this work have been performed on the Joint Fermilab-KICP Supercomputing Cluster, supported by grants from Fermilab, Kavli Institute for Cosmological Physics, and the University of Chicago. This work made extensive use of the NASA Astrophysics Data System and `arXiv.org` preprint server.

APPENDIX

H_2 FORMATION MODEL

In this appendix, we present a complete description of the chemical reaction network of hydrogen and helium, as well as our phenomenological model for the formation of molecular hydrogen. This model differs non-trivially from and supersedes the previous version of this model described in Gnedin et al. (2009).

We follow in detail the eight species of hydrogen and helium: H I, H II, He I, He II, He III, H_2, H^-, and H_2^+. It is not, however, necessary to follow electrons separately, since, in all physical regimes of interest, abundances of H_2^+ and H^- are extremely small, so

$$n_e \approx n_{\rm H\,II} + n_{\rm He\,II} + 2n_{\rm He\,III}.$$

Note that this equation does not include any negative terms and thus n_e will always be calculated with the *relative* error similar to the relative errors of $n_{\rm H\,II}$, $n_{\rm He\,II}$, and $n_{\rm He\,III}$, but not larger.

We follow all other species self-consistently and separately by solving the corresponding ordinary differential equations to avoid potentially unbounded increase of relative error in subtracting abundance of one specie from another (sometimes called "loss of precision"). For example, if the abundance of He III would be calculated by subtracting the abundance of He I and He II from the constant total abundance of He, the relative error of He III can be arbitrarily large when the fraction of He III is small.

We explicitly assume that all species are advected with the same peculiar gas velocity $\vec{v}$. In this case, the equations for the evolution of their number densities can be concisely represented as

$$\frac{\partial n_j}{\partial t} + 3Hn_j + \frac{1}{a}{\rm div}_x(n_j\vec{v}) = \dot{\mathcal{I}}_j + \dot{\mathcal{M}}_j + \dot{\mathcal{D}}_j, \tag{A1}$$

where j = H I, H II, He I, He II, He III, H_2, H^-, and H_2^+, the divergence is taken in comoving space $\vec{x}$, and three terms on the right-hand side include reactions due to ionization balance, molecular chemistry, and dust chemistry, respectively. This subdivision of the reactions into three sets is primarily for the sake of convenience and because we use different sources for different reaction rates. This separation is, of course, artificial—all the reactions take place together in a fluid element.

The OTVET RT solver produces the radiation field at each computational cell that is used to calculate the rates for reactions between chemical species and radiation (including photoionization). We generically label these rates as $\Gamma^{\rm RT}$ with various indices. Since the self-shielding of molecular hydrogen and shielding by dust are not included in the OTVET solver, but are the ingredients of our empirical model, they are encapsulated into two factors, $S_{\rm H_2}$ and $S_{\rm D}$, with which we multiply the appropriate rates. These factors are described below.

A.1. Ionization Balance

Ionization balance terms include standard processes of photoionization, collisional ionization, and radiative recombination, and therefore only involve j = H I, H II, He I, He II, and He III. We label all terms that include at least one of H_2, H^-, and H_2^+ as "molecular chemistry," and describe them all in the following subsection.

$$\begin{cases}
\dot{\mathcal{I}}_{\rm H\,I} &= -n_{\rm H\,I}\Gamma_{\rm H\,I} - C_{\rm H\,I}n_e n_{\rm H\,I} + R_{\rm H\,II}n_e n_{\rm H\,II},\\
\dot{\mathcal{I}}_{\rm H\,II} &= -\dot{\mathcal{I}}_{\rm H\,I} = -R_{\rm H\,II}n_e n_{\rm H\,II} + n_{\rm H\,I}\Gamma_{\rm H\,I} + C_{\rm H\,I}n_e n_{\rm H\,I},\\
\dot{\mathcal{I}}_{\rm He\,I} &= -n_{\rm He\,I}\Gamma_{\rm He\,I} - C_{\rm He\,I}n_e n_{\rm He\,I} + (D_{\rm He\,II} + R_{\rm He\,II})n_e n_{\rm He\,II},\\
\dot{\mathcal{I}}_{\rm He\,II} &= -n_{\rm He\,II}\Gamma_{\rm He\,II} - (D_{\rm He\,II} + R_{\rm He\,II})n_e n_{\rm He\,II} - C_{\rm He\,II}n_e n_{\rm He\,II} + n_{\rm He\,I}\Gamma_{\rm He\,I} + C_{\rm He\,I}n_e n_{\rm He\,I} + R_{\rm He\,III}n_e n_{\rm He\,III},\\
\dot{\mathcal{I}}_{\rm He\,III} &= -R_{\rm He\,III}n_e n_{\rm He\,III} + n_{\rm He\,II}\Gamma_{\rm He\,II} + C_{\rm He\,II}n_e n_{\rm He\,II},\\
\dot{\mathcal{I}}_{\rm H_2} &= \dot{\mathcal{I}}_{\rm H^-} = \dot{\mathcal{I}}_{\rm H_2^+} = 0.
\end{cases} \tag{A2}$$

Here C_j are collisional ionization rates, R_j are radiative recombination rates, and D_j are dielectronic recombination rates. For these rates, we use highly accurate fitting formulae from Hui & Gnedin (1997). The recombination coefficients are computed self-consistently as a combination of case A and case B recombination, depending on the gas opacity.

The photoionization rates are derived from those returned by the RT solver and include the shielding by dust as

$$\begin{cases}
\Gamma_{\rm H\,I} &= S_{\rm D}\Gamma^{\rm RT}_{\rm H\,I} \quad [{\rm H\,I} + \gamma \rightarrow {\rm H\,II}],\\
\Gamma_{\rm He\,I} &= S_{\rm D}\Gamma^{\rm RT}_{\rm He\,I} \quad [{\rm He\,I} + \gamma \rightarrow {\rm He\,II}],\\
\Gamma_{\rm He\,II} &= S_{\rm D}\Gamma^{\rm RT}_{\rm He\,II} \quad [{\rm He\,II} + \gamma \rightarrow {\rm He\,III}].
\end{cases} \tag{A3}$$

In particular, we use the same factor to account for dust shielding in all three photoionization rates. Obviously, this is not exact, as the dust cross section is a function of wavelength. However, since the effect of helium on molecular chemistry inside molecular clouds is thought to be small, helium ionization inside molecular clouds is sufficient to be treated rather approximately.

A.2. Molecular Chemistry

Molecular chemistry terms include a large set of reactions between H_2, H_2^+, and H^- and atomic species. The full set of equations we call "the full eight-species model":

$$\begin{cases}
\dot{\mathcal{M}}_{\rm H\,I} &= \Gamma_A n_{\rm H^-} + \Gamma_B n_{\rm H_2^+} + 2\Gamma_E n_{\rm H_2} + 2\Gamma_{\rm LW} n_{\rm H_2} - k_1 n_e n_{\rm H\,I} - k_2 n_{\rm H^-} n_{\rm H\,I} - k_3 n_{\rm H\,II} n_{\rm H\,I} - k_4 n_{\rm H_2^+} n_{\rm H\,I} \\
&\quad - k_{26} n_{\rm He\,II} n_{\rm H\,I} - 2k_{30} n_{\rm H\,I}^3 - 2k_{31} n_{\rm H\,I}^2 n_{\rm H_2} - 2k_{32} n_{\rm H\,I}^2 n_{\rm He\,I} + 2k_5 n_{\rm H\,II} n_{\rm H^-} + 2k_6 n_e n_{\rm H_2^+} + k_7 n_{\rm H_2} n_{\rm H\,II} \\
&\quad + 2k_8 n_e n_{\rm H_2} + 2k_9 n_{\rm H\,I} n_{\rm H_2} + 2k_{10} n_{\rm H_2} n_{\rm H_2} + 2k_{11} n_{\rm He\,I} n_{\rm H_2} + k_{14} n_e n_{\rm H^-} + k_{15} n_{\rm H\,I} n_{\rm H^-} + k_{21} n_{\rm H_2^+} n_{\rm H^-} \\
&\quad + 3k_{22} n_{\rm H^-} n_{\rm H_2^+} + k_{23} n_e n_{\rm H_2} + k_{24} n_{\rm He\,II} n_{\rm H_2} + k_{27} n_{\rm He\,I} n_{\rm H\,II} + k_{28} n_{\rm He\,II} n_{\rm H^-} + k_{29} n_{\rm He\,I} n_{\rm H^-}, \\
\dot{\mathcal{M}}_{\rm H\,II} &= \Gamma_B n_{\rm H_2^+} + 2\Gamma_C n_{\rm H_2^+} - k_3 n_{\rm H\,I} n_{\rm H\,II} - k_5 n_{\rm H^-} n_{\rm H\,II} - k_7 n_{\rm H_2} n_{\rm H\,II} - k_{16} n_{\rm H^-} n_{\rm H\,II} - k_{27} n_{\rm He\,I} n_{\rm H\,II} + k_4 n_{\rm H_2^+} n_{\rm H\,I} \\
&\quad + k_{24} n_{\rm He\,II} n_{\rm H_2} + k_{26} n_{\rm H\,I} n_{\rm He\,II}, \\
\dot{\mathcal{M}}_{\rm He\,I} &= -k_{27} n_{\rm H\,II} n_{\rm He\,I} - k_{29} n_{\rm H^-} n_{\rm He\,I} + k_{24} n_{\rm He\,II} n_{\rm H_2} + k_{25} n_{\rm He\,II} n_{\rm H_2} + k_{26} n_{\rm He\,II} n_{\rm H\,I} + k_{28} n_{\rm He\,II} n_{\rm H^-}, \\
\dot{\mathcal{M}}_{\rm He\,II} &= -k_{24} n_{\rm H_2} n_{\rm He\,II} - k_{25} n_{\rm H_2} n_{\rm He\,II} - k_{26} n_{\rm H\,I} n_{\rm He\,II} - k_{28} n_{\rm H^-} n_{\rm He\,II} + k_{27} n_{\rm H\,II} n_{\rm He\,I} + k_{29} n_{\rm H^-} n_{\rm He\,I}, \\
\dot{\mathcal{M}}_{\rm He\,III} &= 0, \\
\dot{\mathcal{M}}_{\rm H_2} &= -\Gamma_D n_{\rm H_2} - \Gamma_E n_{\rm H_2} - \Gamma_{\rm LW} n_{\rm H_2} - k_7 n_{\rm H_2} n_{\rm H\,II} - k_8 n_e n_{\rm H_2} - k_9 n_{\rm H\,I} n_{\rm H_2} - k_{10} n_{\rm H_2} n_{\rm H_2} - k_{11} n_{\rm He\,I} n_{\rm H_2} \\
&\quad - k_{23} n_e n_{\rm H_2} - k_{24} n_{\rm He\,II} n_{\rm H_2} - k_{25} n_{\rm He\,II} n_{\rm H_2} + k_2 n_{\rm H^-} n_{\rm H\,I} + k_4 n_{\rm H_2^+} n_{\rm H\,I} + k_{21} n_{\rm H_2^+} n_{\rm H^-} + k_{30} n_{\rm H\,I}^3 \\
&\quad + k_{31} n_{\rm H\,I}^2 n_{\rm H_2} + k_{32} n_{\rm H\,I}^2 n_{\rm He\,I}, \\
\dot{\mathcal{M}}_{\rm H_2^+} &= -\Gamma_B n_{\rm H_2^+} - \Gamma_C n_{\rm H_2^+} + \Gamma_D n_{\rm H_2} - k_4 n_{\rm H\,I} n_{\rm H_2^+} - k_6 n_e n_{\rm H_2^+} - k_{21} n_{\rm H^-} n_{\rm H_2^+} - k_{22} n_{\rm H^-} n_{\rm H_2^+} + k_3 n_{\rm H\,I} n_{\rm H\,II} \\
&\quad + k_7 n_{\rm H_2} n_{\rm H\,II} + k_{16} n_{\rm H\,II} n_{\rm H^-} + k_{25} n_{\rm H_2} n_{\rm He\,II}, \\
\dot{\mathcal{M}}_{\rm H^-} &= -\Gamma_A n_{\rm H^-} - k_2 n_{\rm H\,I} n_{\rm H^-} - k_5 n_{\rm H\,II} n_{\rm H^-} - k_{14} n_e n_{\rm H^-} - k_{15} n_{\rm H\,I} n_{\rm H^-} - k_{16} n_{\rm H\,II} n_{\rm H^-} - k_{21} n_{\rm H_2^+} n_{\rm H^-} - \\
&\quad - k_{22} n_{\rm H_2^+} n_{\rm H^-} - k_{28} n_{\rm He\,II} n_{\rm H^-} - k_{29} n_{\rm He\,I} n_{\rm H^-} + k_1 n_e n_{\rm H\,I} + k_{23} n_e n_{\rm H_2},
\end{cases} \tag{A4}$$

where

$$\begin{cases}
\Gamma_A &= S_D \Gamma_A^{\rm RT} & [{\rm H^-} + \gamma \rightarrow {\rm H\,I} + e], \\
\Gamma_B &= S_D \Gamma_B^{\rm RT} & [{\rm H_2^+} + \gamma \rightarrow {\rm H\,I} + {\rm H\,II}], \\
\Gamma_C &= S_D \Gamma_C^{\rm RT} & [{\rm H_2^+} + \gamma \rightarrow 2{\rm H\,II} + e], \\
\Gamma_D &= S_D S_{\rm H_2} \Gamma_D^{\rm RT} & [{\rm H_2} + \gamma \rightarrow {\rm H_2^+} + e], \\
\Gamma_E &= S_D S_{\rm H_2} \Gamma_E^{\rm RT} & [{\rm H_2} + \gamma \rightarrow 2{\rm H\,I}\ (h\nu > 13.6\,{\rm eV})], \\
\Gamma_{\rm LW} &= S_D S_{\rm H_2} \Gamma_{\rm LW}^{\rm RT} & [{\rm H_2} + \gamma \rightarrow 2{\rm H\,I}\ ({\rm Lyman\text{–}Werner\ band})].
\end{cases} \tag{A5}$$

The rate coefficients k_1–k_{32} are taken from Glover & Abel (2008); we do not list here all these reactions for brevity. Cross sections for photorates A–D are given by Shapiro & Kang (1987), while the cross section for the reaction E is given by Abel et al. (1997), for both ortho- and para-H_2. The RT in the Lyman–Werner bands $\Gamma_{\rm LW}^{\rm RT}$ is treated fully self-consistently with 20,000 frequency bins, as described in Ricotti et al. (2002).

Analogously to the previous section, we use the same $S_{\rm H_2}$ factor to account for H_2 self-shielding for reactions D, E, and LW. This is a crude approximation, but a more accurate treatment would introduce additional parameters that cannot yet be calibrated with the existing limited observational measurements.

Equations (A4) can be substantially simplified if we note that in all physical regimes relevant to cosmology the abundances of H_2^+ and H^- are always extremely small, so that they can always be assumed to be in the kinetic equilibrium, $\dot{\mathcal{M}}_{\rm H_2^+} \approx \dot{\mathcal{M}}_{\rm H^-} \approx 0$ (T. Abel 2006, private communication). With this assumption and neglecting reactions involving k_{21} and k_{22}, because their rates are $\propto n_{\rm H^-} n_{\rm H_2^+}$ where both $n_{\rm H^-}$ and $n_{\rm H_2^+}$ are small, expressions for the equilibrium abundances of H_2^+ and H^- can be derived in a closed form, resulting in the following "six-species model":

$$\begin{cases}
n_{\rm H^-} &= \dfrac{k_1 n_e n_{\rm H\,I} + k_{23} n_e n_{\rm H_2}}{\Gamma_A + k_2 n_{\rm H\,I} + k_5 n_{\rm H\,II} + k_{14} n_e + k_{15} n_{\rm H\,I} + k_{16} n_{\rm H\,II} + k_{28} n_{\rm He\,II} + k_{29} n_{\rm He\,I}}, \\
n_{\rm H_2^+} &= \dfrac{\Gamma_D n_{\rm H_2} + k_3 n_{\rm H\,I} n_{\rm H\,II} + k_7 n_{\rm H_2} n_{\rm H\,II} + k_{16} n_{\rm H\,II} n_{\rm H^-} + k_{25} n_{\rm H_2} n_{\rm He\,II}}{\Gamma_B + \Gamma_C + k_4 n_{\rm H\,I} + k_6 n_e}, \\
\dot{\mathcal{M}}_{\rm H\,I} &= \Gamma_A n_{\rm H^-} + \Gamma_B n_{\rm H_2^+} + 2\Gamma_E n_{\rm H_2} + 2\Gamma_{\rm LW} n_{\rm H_2} - k_1 n_e n_{\rm H\,I} - k_2 n_{\rm H^-} n_{\rm H\,I} - k_3 n_{\rm H\,II} n_{\rm H\,I} - k_4 n_{\rm H_2^+} n_{\rm H\,I} \\
&\quad - k_{26} n_{\rm He\,II} n_{\rm H\,I} - 2k_{30} n_{\rm H\,I}^3 - 2k_{31} n_{\rm H\,I}^2 n_{\rm H_2} - 2k_{32} n_{\rm H\,I}^2 n_{\rm He\,I} + 2k_5 n_{\rm H\,II} n_{\rm H^-} + 2k_6 n_e n_{\rm H_2^+} + k_7 n_{\rm H_2} n_{\rm H\,II} \\
&\quad + 2k_8 n_e n_{\rm H_2} + 2k_9 n_{\rm H\,I} n_{\rm H_2} + 2k_{10} n_{\rm H_2} n_{\rm H_2} + 2k_{11} n_{\rm He\,I} n_{\rm H_2} + k_{14} n_e n_{\rm H^-} + k_{15} n_{\rm H\,I} n_{\rm H^-} \\
&\quad + k_{23} n_e n_{\rm H_2} + k_{24} n_{\rm He\,II} n_{\rm H_2} + k_{27} n_{\rm He\,I} n_{\rm H\,II} + k_{28} n_{\rm He\,II} n_{\rm H^-} + k_{29} n_{\rm He\,I} n_{\rm H^-}, \\
\dot{\mathcal{M}}_{\rm H\,II} &= \Gamma_B n_{\rm H_2^+} + 2\Gamma_C n_{\rm H_2^+} - k_3 n_{\rm H\,I} n_{\rm H\,II} - k_5 n_{\rm H^-} n_{\rm H\,II} - k_7 n_{\rm H_2} n_{\rm H\,II} - k_{16} n_{\rm H^-} n_{\rm H\,II} - k_{27} n_{\rm He\,I} n_{\rm H\,II} + k_4 n_{\rm H_2^+} n_{\rm H\,I} \\
&\quad + k_{24} n_{\rm He\,II} n_{\rm H_2} + k_{26} n_{\rm H\,I} n_{\rm He\,II}, \\
\dot{\mathcal{M}}_{\rm He\,I} &= -k_{27} n_{\rm H\,II} n_{\rm He\,I} - k_{29} n_{\rm H^-} n_{\rm He\,I} + k_{24} n_{\rm He\,II} n_{\rm H_2} + k_{25} n_{\rm He\,II} n_{\rm H_2} + k_{26} n_{\rm He\,II} n_{\rm H\,I} + k_{28} n_{\rm He\,II} n_{\rm H^-}, \\
\dot{\mathcal{M}}_{\rm He\,II} &= -k_{24} n_{\rm H_2} n_{\rm He\,II} - k_{25} n_{\rm H_2} n_{\rm He\,II} - k_{26} n_{\rm H\,I} n_{\rm He\,II} - k_{28} n_{\rm H^-} n_{\rm He\,II} + k_{27} n_{\rm H\,II} n_{\rm He\,I} + k_{29} n_{\rm H^-} n_{\rm He\,I}, \\
\dot{\mathcal{M}}_{\rm He\,III} &= 0, \\
\dot{\mathcal{M}}_{\rm H_2} &= -\Gamma_D n_{\rm H_2} - \Gamma_E n_{\rm H_2} - \Gamma_{\rm LW} n_{\rm H_2} - k_7 n_{\rm H_2} n_{\rm H\,II} - k_8 n_e n_{\rm H_2} - k_9 n_{\rm H\,I} n_{\rm H_2} - k_{10} n_{\rm H_2} n_{\rm H_2} - k_{11} n_{\rm He\,I} n_{\rm H_2} \\
&\quad - k_{23} n_e n_{\rm H_2} - k_{24} n_{\rm He\,II} n_{\rm H_2} - k_{25} n_{\rm He\,II} n_{\rm H_2} + k_2 n_{\rm H^-} n_{\rm H\,I} + k_4 n_{\rm H_2^+} n_{\rm H\,I} + k_{30} n_{\rm H\,I}^3 + k_{31} n_{\rm H\,I}^2 n_{\rm H_2} + k_{32} n_{\rm H\,I}^2 n_{\rm He\,I}.
\end{cases} \tag{A6}$$

Finally, under normal ISM conditions the ionization balance of hydrogen and helium is controlled by the radiative recombination, photoionization, and ionization by cosmic rays. In this limit, we can ignore all gas-phase molecular chemistry reactions,

$$\dot{\mathcal{M}}_j \approx 0.$$

We dub this approximation the "*minimal model.*" The minimal model is often (justifiably) used in studies of local ISM (cf. Krumholz & McKee 2005; Pelupessy et al. 2006; Krumholz & Tan 2007; Glover & Mac Low 2007a, 2007b), but is also occasionally applied to high-redshift or low-metallicity systems (Krumholz et al. 2009a; Pelupessy & Papadopoulos 2009). We find, however, that the minimal model produces results that are reasonably close to the full model for $D_{\rm MW} \gtrsim 0.01$ (for any FUV flux), but becomes progressively less accurate for lower dust-to-gas ratios, mispredicting the atomic-to-molecular transition as a function of density by a factor of two for $D_{\rm MW} \sim 0.01$.

In order to maintain high accuracy for the full sampled range of $D_{\rm MW}$ and $U_{\rm MW}$, all simulations presented in this paper were performed with the six-species model.

A.3. Dust Chemistry

In our model, the only dust chemistry reaction that we include is the formation of molecular hydrogen on dust,

$$\begin{cases} \dot{\mathcal{D}}_{\rm H_2} &= D_{\rm MW} R_0 C_\rho n_{\rm H\,I} (n_{\rm H\,I} + 2 n_{\rm H_2}), \\ \dot{\mathcal{D}}_{\rm H\,I} &= -2 \dot{\mathcal{D}}_{\rm H_2}, \\ \dot{\mathcal{D}}_{\rm H\,II} &= \dot{\mathcal{D}}_{\rm He\,I} = \dot{\mathcal{D}}_{\rm He\,II} = \dot{\mathcal{D}}_{\rm He\,III} = \dot{\mathcal{D}}_{\rm H^-} = \dot{\mathcal{D}}_{\rm H_2^+} = 0, \end{cases} \tag{A7}$$

where $R_0 = 3.5 \times 10^{-17}$ cm^3 s^{-1} (Wolfire et al. 2008; see Equation (1)) and C_ρ is the clumping factor inside molecular clouds, which takes into account the fact that the gas is clumped on subgrid scales unresolved in our simulations (also see Gnedin et al. 2009). The clumping factor C_ρ is a parameter of our model, we discuss a reasonable choice for its value below, in Section A.7.

A.4. Heating, Cooling, and Thermodynamics

For the heating and cooling terms in the equation for the internal energy, we include all of the terms normally included in the simulations of first stars and in the ISM models. Specifically, the entropy equation for the gas can be written as

$$\rho T \frac{ds}{dt} = \dot{\mathcal{H}} - \dot{\mathcal{C}},$$

where $\dot{\mathcal{H}}$ and $\dot{\mathcal{C}}$ are heating and cooling terms,

$$\dot{\mathcal{H}} = \dot{\mathcal{H}}_{\rm PI} + \dot{\mathcal{H}}_{\rm CMB} + \dot{\mathcal{H}}_{\rm Ly\alpha} + \dot{\mathcal{H}}_{\rm H_2} + \dot{\mathcal{H}}_{\rm PAH} + \dot{\mathcal{H}}_{\rm CR},$$

$$\dot{\mathcal{C}} = \dot{\mathcal{C}}_{\rm CI} + \dot{\mathcal{C}}_{\rm RR} + \dot{\mathcal{C}}_{\rm DER} + \dot{\mathcal{C}}_{\rm LE,A} + \dot{\mathcal{C}}_{\rm FF} + \dot{\mathcal{C}}_{\rm QX} + \dot{\mathcal{C}}_{\rm LE,H_2} + \dot{\mathcal{C}}_{\rm LE,Z} + \dot{\mathcal{C}}_{\rm D}. \tag{A8}$$

In the heating function, we include the following:

$\dot{\mathcal{H}}_{\rm PI}$: photoionization heating due to H I, He I, and He II, using cross sections from Hui & Gnedin (1997);

$\dot{\mathcal{H}}_{\rm CMB}$: Compton heating/cooling on the cosmic microwave background (Hui & Gnedin 1997);

$\dot{\mathcal{H}}_{\rm Ly\alpha}$: heating by Ly$\alpha$ photons (Tozzi et al. 2000);

$\dot{\mathcal{H}}_{\rm H_2}$: heating due to photodissociation of H_2, $\dot{\mathcal{H}}_{\rm H_2} = 0.4\,{\rm eV} \times n_{\rm H_2} (\Gamma_{\rm D} + \Gamma_{\rm E} + \Gamma_{\rm LW})$ (Equation (A5));

$\dot{\mathcal{H}}_{\rm PAH}$: photoelectric heating on polycyclic aromatic hydrocarbons, implemented as in Glover & Mac Low (2007a);

$\dot{\mathcal{H}}_{\rm CR}$: cosmic rate heating, assuming that the cosmic rate density scales as the dust-to-gas ratio, implemented as in Glover & Mac Low (2007a).

Cooling processes include the following:

$\dot{\mathcal{C}}_{\rm CI}$: cooling due to collisional ionizations of H I, He I, and He II (Hui & Gnedin 1997);

$\dot{\mathcal{C}}_{\rm RR}$: cooling due to radiative recombinations of H II, He II, and He III (Hui & Gnedin 1997);

$\dot{\mathcal{C}}_{\rm DER}$: cooling due to dielectronic recombination of He III (Hui & Gnedin 1997);

$\dot{\mathcal{C}}_{\rm LE,A}$: line excitation cooling of H I and He II (Hui & Gnedin 1997);

$\dot{\mathcal{C}}_{\rm FF}$: free–free emission (Hui & Gnedin 1997);

$\dot{\mathcal{C}}_{\rm QX}$: cooling due to charge exchange reactions between H_2, H^-, H I, and free electrons (reactions 8, 9, 10, 14, and 15 from Glover & Abel 2008);

$\dot{\mathcal{C}}_{\rm LE,H_2}$: line excitation cooling of H_2 (Glover & Abel 2008);

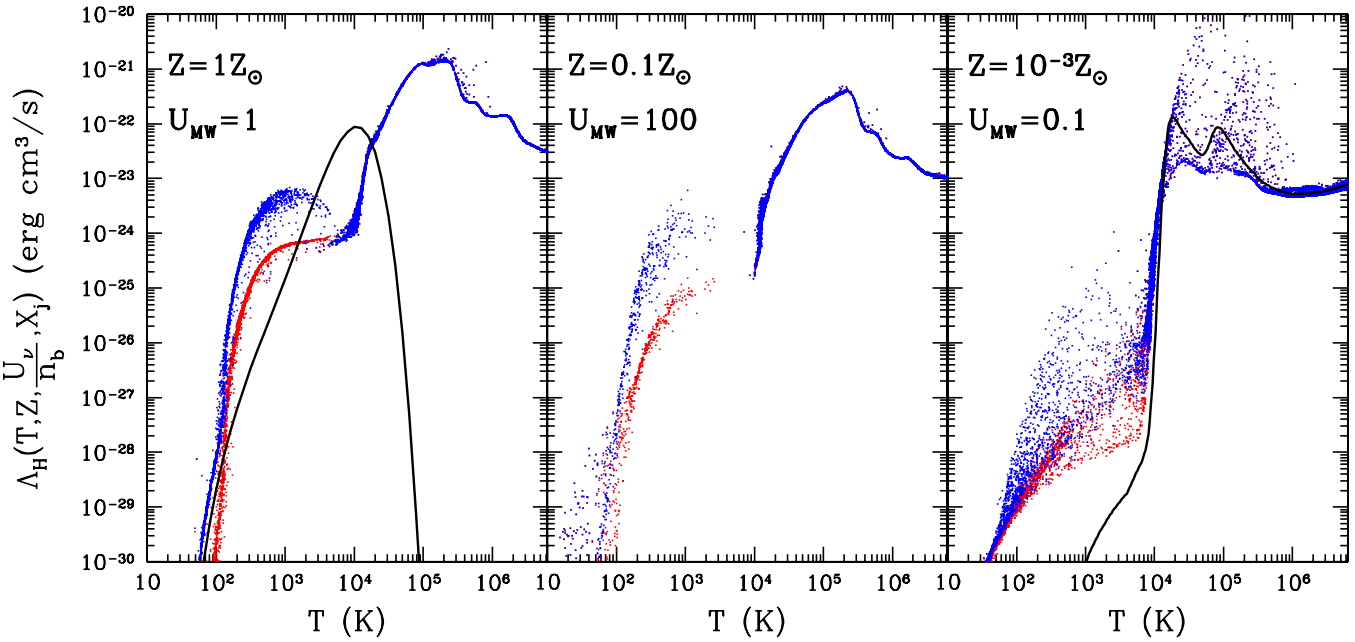

Figure 10. Cooling functions (per hydrogen nucleus) for three representative values of gas metallicity Z and the FUV flux $U_{\rm MW}$. In this plot, we assume $D_{\rm MW} = Z/Z_\odot$. Blue points show the full cooling function (including all relevant physical processes), while red points show the result of excluding H_2 cooling. Black lines trace the H_2 cooling function from Galli & Palla (1998; left panel) and the standard, metal-free cooling function (right panel).

(A color version of this figure is available in the online journal.)

$\dot{\mathcal{C}}_{{\rm LE},Z}$: line excitation cooling of heavy elements, using Sutherland & Dopita (1993) cooling functions for $T > 10^4$ K and Penston (1970) and Dalgarno & McCray (1972) rates in the $T < 10^4$ K regime;

$\dot{\mathcal{C}}_{\rm D}$: cooling on dust from Draine (1981).

Some of the reaction rates involving H_2 depend on the ortho-to-para ratio of molecular hydrogen. For this ratio and other thermodynamic quantities ($\gamma(T)$, $U(T)$, etc.), we use exact expressions computed from quantum-mechanical statistical sums (M. Turk et al. 2011, in preparation).

Examples of cooling functions from our simulations are given in Figure 10. The cooling function, in general, is *not* a function of gas temperature only, but also depends on the gas metallicity Z, the energy density of the incident radiation field U_ν, the number density of baryons n_b (although for $n_b \lesssim 10^4$ cm^{-3} the dependence on the last two parameters always enters as U_ν/n_b), and abundances of all atomic and molecular species $X_j \equiv n_j/n_b$. Therefore, when plotted as a function of temperature, the cooling function takes a range of values (depending on the values of other gas properties) rather than a single, unique value.

Interestingly, Figure 10 shows that the cooling rate at $T < 10^4$ K is dominated by cooling due to molecular hydrogen, rather than by low ionization metal species such as O I or C II, as is commonly assumed. Molecular hydrogen cooling is often assumed to be negligible (cf. Wolfire et al. 2003; Stahler & Palla 2005) due to lower cooling rates (cf. Galli & Palla 1998). However, we use the updated H_2 cooling rates of Glover & Abel (2008), which are considerably higher than the previous estimates. As Figure 10 shows, the new H_2 cooling rates dominate over the low ionization metal species at $T \lesssim 5000$ K.

A.5. Shielding Factors

The two shielding factors, $S_{\rm D}$ and $S_{\rm H_2}$, together with the clumping factor C_ρ, are important parameters of our empirical model. As Gnedin et al. (2009) explain, we use an ansatz similar in spirit to the Sobolev approximation to estimate dust shielding:

$$S_{\rm D} = e^{-D_{\rm MW}\sigma_0(n_{\rm H\,I} + 2n_{\rm H_2})L_{\rm Sob}}, \tag{A9}$$

where $D_{\rm MW}$ is the dust-to-gas ratio in units of its MW value (see Section 2), $\sigma_0 = 2 \times 10^{-21}$ cm^2, and

$$L_{\rm Sob} \equiv \rho/(2|\nabla\rho|). \tag{A10}$$

Note that the value for σ_0 that we use in this paper is twice lower than the one listed in Gnedin et al. (2009); the new value is a commonly adopted value for this parameter for the MW-type dust and provides a better quantitative fit to the existing observational constraints. In addition, a factor of two in the denominator of the expression for $L_{\rm Sob}$ was missing in Gnedin et al. (2009)—this was a typo, and the correct expression was used when simulations were run.

The major change between our current model and the model of Gnedin et al. (2009) is in the form of the molecular hydrogen self-shielding factor. In Gnedin et al. (2009), this form was modified from the commonly used formula of Draine & Bertoldi (1996),

because the FUV flux in Gnedin et al. (2009) was much higher than the Draine value. In our present tests, we find that we can use either the original Draine & Bertoldi (1996) formula or their simpler and more approximate expression,

$$S_{\rm H_2} = \begin{cases} 1, & \text{for } N_{\rm H_2} < 10^{14}\,{\rm cm}^{-2}, \\ (N_{\rm H_2}/10^{14}\,{\rm cm}^{-2})^{-3/4}, & \text{for } N_{\rm H_2} > 10^{14}\,{\rm cm}^{-2}, \end{cases} \tag{A11}$$

which we actually use for computational efficiency.[6]

Finally, to complete the full specification of our chemical model, we need to estimate the column density of the molecular gas, $N_{\rm H_2}$, for the self-shielding factor given by Equation (A11). Unfortunately, we cannot simply use the Sobolev approximation to derive $N_{\rm H_2}$ similar to the column density of dust in Equation (A9), because H_2 absorption is concentrated in separate absorption lines and is sensitive to the internal velocity dispersion inside molecular clouds. These velocities are unresolved in our simulations, but can greatly reduce the self-shielding of molecular gas. Dust, on the other hand, absorbs UV radiation in continuum and is thus not affected by velocity distribution of the gas.

Therefore, we introduce the following simple ansatz for the effective column density $N_{\rm H_2}$ for Equation (A11),

$$N_{\rm H_2} \approx n_{\rm H_2} L_c, \tag{A12}$$

where L_c is the velocity coherence length of the molecular hydrogen inside molecular clouds. Since we cannot deduce this quantity from observations or other calculations, we treat it as another parameter of our model.

With the expressions for the shielding factors above, the only two parameters of our model are C_ρ and L_c. These parameters can only be determined by comparing the simulation results to the observational data.

A.6. Correction for Numerical Diffusion

Ideally, in a simulation with infinite spatial resolution, our model should work as designed. In practice, however, the spatial resolution of a simulation is finite. In addition, numerical solutions of partial differential equations always contain truncation errors. As Gnedin et al. (2009) show, these errors lead to a small, but non-negligible amount of numerical heating and advection that biases the H_2 formation model.

The analysis of this numerical diffusion bias and the method to correct it in our simulations is described in detail in Gnedin et al. (2009). Here we only list all the relevant equations for the sake of completeness.

The correction procedure consists in multiplying the densities of H I and H II and the gas temperature T that are returned by the hydro solver—$n^{\rm HS}_{\rm H\,I}$, $n^{\rm HS}_{\rm H\,II}$, and $T^{\rm HS}$ (and which are used as initial conditions to Equations (A1))—by the following correction factors,

$$n^{\rm HS}_{\rm H\,I} \to \frac{n^{\rm HS}_{\rm H\,I}}{1 + Q_{\rm Num}\left(n_{\rm H}/n^{\rm HS}_{\rm H\,I}\right)},$$

$$n^{\rm HS}_{\rm H\,II} \to \frac{n^{\rm HS}_{\rm H\,II}}{1 + Q_{\rm Num}\left(n_{\rm H}/n^{\rm HS}_{\rm H\,II}\right)},$$

$$T^{\rm HS} \to \frac{T^{\rm HS}}{1 + Q_{\rm Num}(T/30\,{\rm K})},$$

while simultaneously adjusting the density of molecular hydrogen to ensure mass conservation. The correction factor $Q_{\rm Num}$ is defined as

$$Q_{\rm Num} \equiv \alpha\sigma_{\rm cell}\frac{\Delta t}{\Delta x}\left(1 - S_D^{1/3}\right),$$

where α is a numerical coefficient of the order of unity, $\sigma_{\rm cell}$ is the gas velocity dispersion at the cell scale, computed in each cell (i, j, k) from its six neighbors,

$$\sigma^2_{\rm cell}(i, j, k) \equiv \frac{1}{6}[(\vec{v}_{i+1,j,k} - \vec{v}_{i,j,k})^2 + (\vec{v}_{i-1,j,k} - \vec{v}_{i,j,k})^2 + (\vec{v}_{i,j+1,k} - \vec{v}_{i,j,k})^2 + \cdots],$$

where Δt and Δx are the numerical time step and the cell size (which is, in fact, different for different cells on an adaptively refined mesh in our simulations), and the factor $1 - S_D^{1/3}$ ensures that the numerical correction becomes non-trivial only when the dust shielding is strong ($S_D \ll 1$, i.e., inside molecular clouds). This last factor was not included in the numerical correction formula of Gnedin et al. (2009); in this paper, we find that we can reduce the numerical correction by that factor without noticeably biasing the H_2 formation model.

This form for the numerical correction is rather insensitive to the specific choice of the coefficient α: varying α from 0.5 to 2 changes atomic hydrogen fractions inside molecular clouds and SFRs by less than their natural scatter. We use $\alpha = 1$ as the fiducial value.

[6] We have indeed verified that a more complex formula (Equation (37) of Draine & Bertoldi 1996) produces essentially indistinguishable results from the more approximate form of Equation (A11).

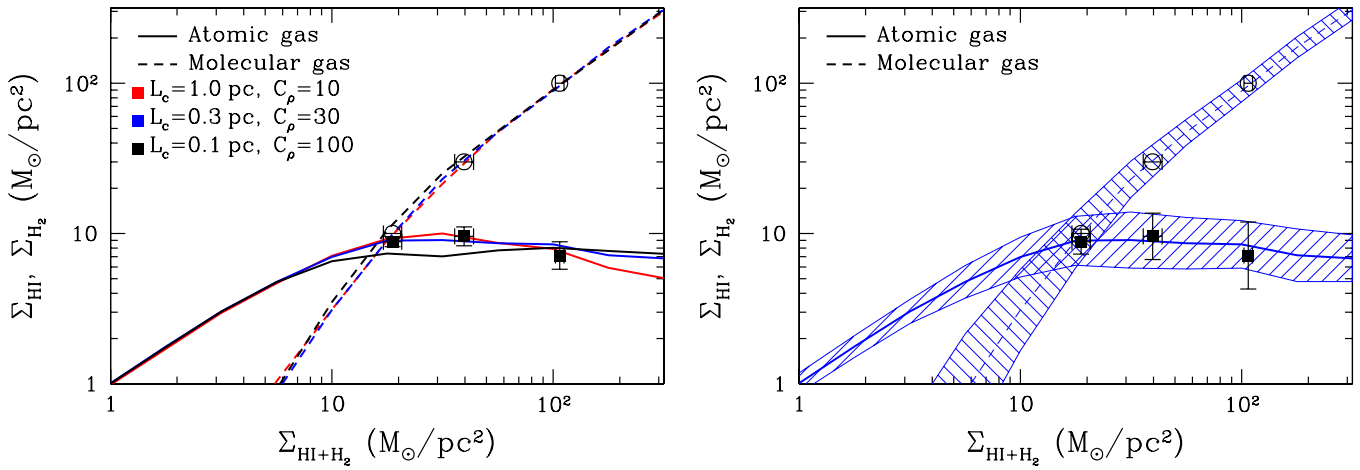

Figure 11. Average atomic and molecular gas surface densities as functions of the total (neutral) hydrogen gas surface density averaged over 500 pc scale. The left panel shows three test simulations with three values of the clumping factor C_ρ and molecular coherence length L_c. Filled squares and open circles with error bars mark the observed average atomic and molecular hydrogen surface densities at $\Sigma_{H_2} = 10$, 30, and 100 $M_\odot$ pc^{-2} from Wong & Blitz (2002). The right panel shows our fiducial model ($L_c = 0.3$ pc, $C_\rho = 30$) together with the rms scatter (shaded bands) around the averages. The error bars on the observational points now show the dispersion around the average rather than the error of the mean.

(A color version of this figure is available in the online journal.)

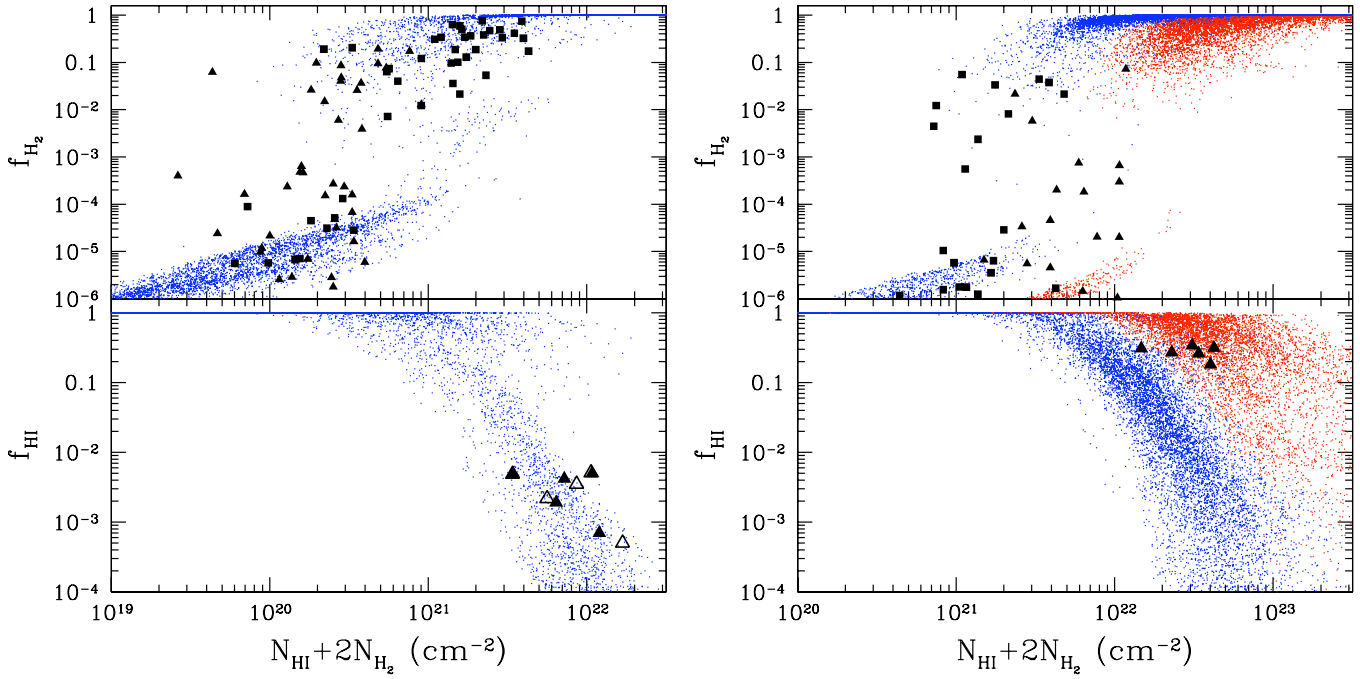

Figure 12. Atomic (bottom) and molecular (top) gas fractions as functions of the total (neutral) hydrogen gas column density along individual lines of sight through the galactic disks. Colored points show our fiducial test simulation ($L_c = 0.3$ pc, $C_\rho = 30$), while black points show observational measurements. The left panel shows the ($D_{MW} = 1$, $U_{MW} = 1$) simulation case and the observational measurements of molecular fractions in the MW galaxy from Gillmon et al. (2006; filled triangles) and Wolfire et al. (2008; filled squares) and atomic fractions measurements from Goldsmith & Li (2005). The right panel shows ($D_{MW} = 0.3$, $U_{MW} = 10$; blue points) and ($D_{MW} = 0.1$, $U_{MW} = 100$; red points) simulation cases that should bracket possible values of these parameters for Magellanic Clouds. Filled squares and triangles on the top panel show the measurements for LMC and SMC molecular fractions, respectively (Tumlinson et al. 2002). On the bottom panel, the measurements are for SMC (Leroy et al. 2007) to be compared with red points.

(A color version of this figure is available in the online journal.)

A.7. Calibration

As the primary data sets used to calibrate the model, we use the measurements of atomic and molecular gas surface densities in nearby spirals from Wong & Blitz (2002) in Figure 11 and measurements of gas fractions along the lines of sight to individual stars for atomic (Goldsmith & Li 2005) and molecular gas in the MW and Magellanic Clouds (Tumlinson et al. 2002; Gillmon et al. 2006; Wolfire et al. 2008) in Figure 12.

We calibrate the two parameters of the model: the clumping factor C_ρ and the molecular coherence length L_c. We find, however, that there is no unique best-fit set of parameters. Instead, any combination of these two parameters that satisfy the constraint

$$L_c C_\rho \approx 10 \text{ pc}$$

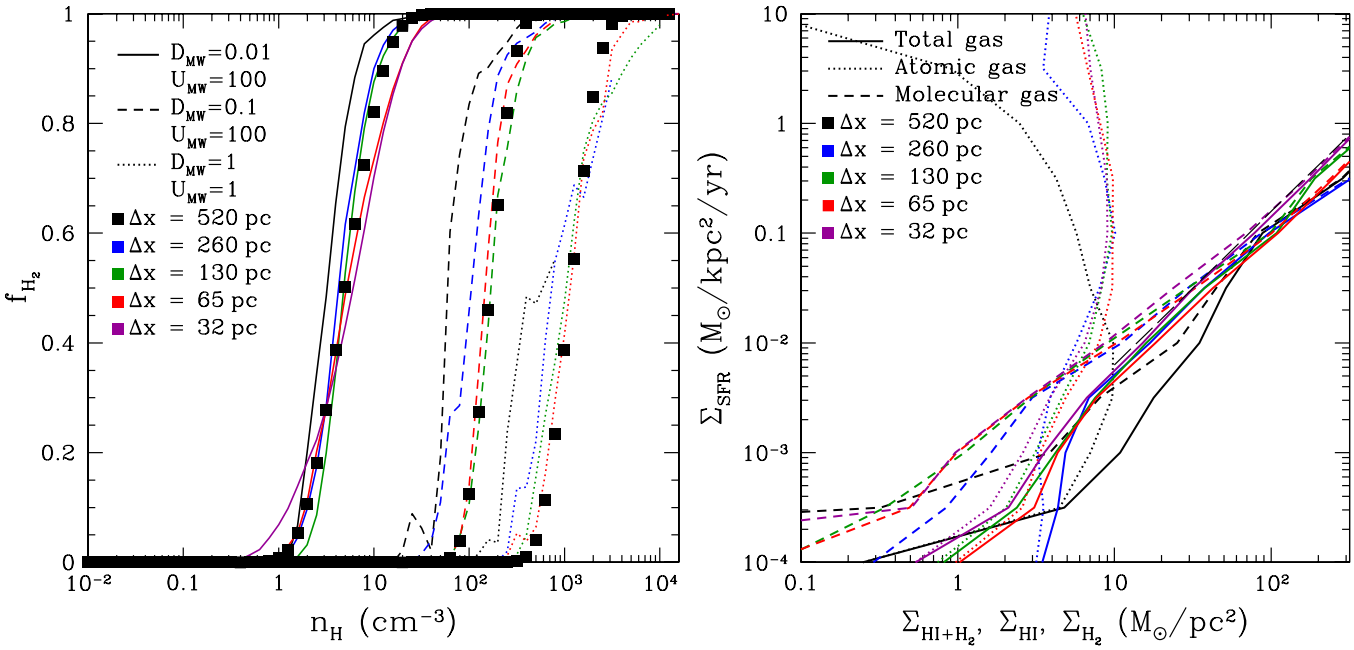

Figure 13. Dependence of the atomic-to-molecular transition (left) and the K-S relation (right) on numerical resolution in our model. The left panel shows three representative cases $(D_{\rm MW}, U_{\rm MW}) = (1, 1)$, $(D_{\rm MW}, U_{\rm MW}) = (0.1, 100)$, and $(D_{\rm MW}, U_{\rm MW}) = (0.01, 100)$, while only the first case (MW-like parameters) is shown on the right panel for the sake of clarity (the other two cases show similar behavior). The value of the cell size Δx on the highest resolved level is shown for each line. Black squares on the left panel trace the approximate fit (6). Note that we ran only one case (MW-like parameters) with the highest resolution (32 pc) because of computational expense.

(A color version of this figure is available in the online journal.)

provides an acceptable fit to the observational constraints. As an example, we show in the left panel of Figure 11 fits to the Wong & Blitz (2002) measurements (averaged over all galaxies they observed) for three combinations of the parameters L_c and C_ρ. In general, higher clumping factors result in the lower atomic contents at high surface densities, but the trend is too weak to be of any statistically significant constraining power.

As a fiducial set of parameters we choose the combination $L_c = 0.3$ pc and $C_\rho = 30$. This choice provides a marginally better overall fit to the observations and is also consistent with estimates of the gas clumping factor deep inside molecular clouds (McKee & Ostriker 2007). The fiducial value of C_ρ is somewhat larger than the estimates of the clumping factor from numerical simulations of turbulent molecular clouds, $C_\rho = e^{\sigma^2_{\ln\rho}}$, where $\sigma_{\ln\rho} \approx 1$–$1.5$ is the dispersion of the lognormal density distribution inside the clouds. However, the value of $C_\rho = 10$, which was used in Gnedin et al. (2009) and is more consistent with the numerical simulations of turbulent molecular clouds would provide an almost equally good to the existing observations, if it is used with $L_c \approx 1$ pc.

A.8. Dependence on Numerical Resolution

Any sub-cell model would be of limited value, if it was only applicable to a narrow range of numerical resolutions. In order to test the range of spatial resolutions over which our model performs robustly, we have re-run a subset of our test simulations, varying the maximum allowed level of refinement between 6 and 10, compared to our fiducial value of 9 (cell size of $\Delta x = 65$ pc at $z = 3$ in physical units).

The results of these tests are shown in Figure 13 for the atomic-to-molecular transition and the K-S relation. In order to perform a genuine resolution test, in each run with different resolution we only show cells that are refined to the lowest allowed level. For example, in the run with the maximum level 10, we only show cells from level 10, so that level 9 cells, which are also present in that test run, do not contaminate Figure 13. Of course, in realistic simulations cells from all levels that contain molecular gas are going to contribute to the $f_{\rm H_2}$–$n_{\rm H}$ relation, so Figure 13 actually *exaggerates* the effect of changing resolution. At resolutions $\Delta x \lesssim 260$ pc our model performs robustly down to the smallest scales we are able to probe ($\Delta x \approx 30$ pc). At coarser resolution of $\Delta x = 520$ pc small molecular clouds in low-density gas are not captured properly, resulting in a sharper falloff in the K-S relation at low values of $\Sigma_{\rm H\,I+H_2}$. In addition, the Sobolev-like approximation for the dust column density (Equation (A10)) overestimates the column density significantly, which results in the atomic-to-molecular transition shifting toward lower density gas (especially for low dust-to-gas ratio and high FUV flux). We conclude, therefore, that spatial resolution of at least 250 pc is required for our model to work robustly.

A.9. Dependence on Averaging Scales

The exact value of the SFR surface density and the gas surface density in principle can depend on the specific choices for the spatial and temporal scales over which $\Sigma_{\rm H}$ and $\Sigma_{\rm SFR}$ are averaged. Observational studies (Kennicutt 1998; Salim et al. 2007; Bigiel et al. 2008) often use a combination of star formation estimators that correspond to different temporal scales. Therefore, the best approach would be to model the observational methodology exactly, but this is not feasible in practice. In this paper, we adopt a simplified

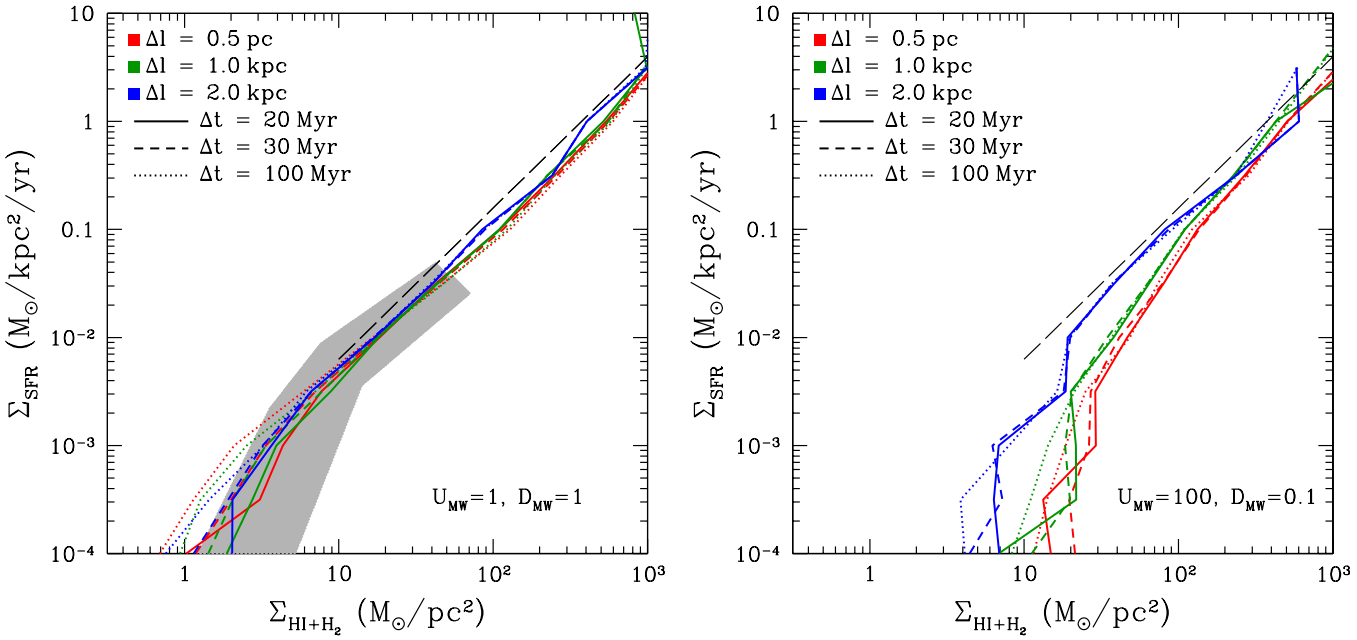

Figure 14. Dependence of the K-S relation on the spatial and temporal scales over which the SFR is averaged for two representative sets of parameters: $U_{\rm MW} = 1$, $D_{\rm MW} = 1$ (left panel) and $U_{\rm MW} = 100$, $D_{\rm MW} = 0.1$ (right panel). Line types and colors show averaging over spatial scales from 500 pc to 2 kpc and over time period from 20 Myr to 100 Myr.

(A color version of this figure is available in the online journal.)

procedure and select the fixed values for both the temporal Δt and spatial Δl averaging scales. The sensitivity of our results to the exact choice for these two scales is shown in Figure 14. In general, the K-S relations measured in the simulations are robust for $\Delta t \lesssim 30$ Myr and $\Delta l \lesssim 1$ kpc. For larger spatial and temporal scales, the modest trends are observed. Several processes can contribute to such trends. For example, if the star formation at low surface densities is intermittent on the timescale of the averaging (i.e., stars form only during episodes of duration comparable to the averaging time period), the average $\Sigma_{\rm SFR}$ can depend on the time period used for averaging. This may explain the weak trend at low $\Sigma_{\rm H}$ with Δt. Such trend is also consistent with observations (e.g., Boissier et al. 2007), which show that star formation derived from the UV flux is more spatially extended compared to the star formation derived from H_α, which corresponds to time period of $\sim 10^7$ yr. Overall, our results are quite robust to changes of spatial and temporal averaging scales within the range of values used in observations. This relative insensitivity of the K-S relation (besides the weak trends mentioned above) is in general agreement with observations, which indicate broadly consistent K-S relations derived using different star formation indicators and a wide range of spatial averaging scales (e.g., Kennicutt et al. 2007; Bigiel et al. 2008).

REFERENCES

Abel, T., Anninos, P., Zhang, Y., & Norman, M. L. 1997, New Astron., 2, 181
Agertz, O., Teyssier, R., & Moore, B. 2011, MNRAS, 410, 1391
Bigiel, F., Leroy, A., Walter, F., Brinks, E., de Blok, W. J. G., Madore, B., & Thornley, M. D. 2008, AJ, 136, 2846
Boissier, S., Prantzos, N., Boselli, A., & Gavazzi, G. 2003, MNRAS, 346, 1215
Boissier, S., et al. 2007, ApJS, 173, 524
Boissier, S., et al. 2008, ApJ, 681, 244
Calura, F., Pipino, A., & Matteucci, F. 2008, A&A, 479, 669
Collins, J. A., Rand, R. J., Duric, N., & Walterbos, R. A. M. 2000, ApJ, 536, 645
Dalgarno, A., & McCray, R. A. 1972, ARA&A, 10, 375
Das, M., O'Neil, K., Vogel, S. N., & McGaugh, S. 2006, ApJ, 651, 853
Dolphin, A. E., Weisz, D. R., Skillman, E. D., & Holtzman, J. A. 2005, arXiv:astro-ph/0506430
Draine, B. T. 1978, ApJS, 36, 595
Draine, B. T. 1981, ApJ, 245, 880
Draine, B. T., & Bertoldi, F. 1996, ApJ, 468, 269
Draine, B. T., et al. 2007, ApJ, 663, 866
Dutton, A. A., van den Bosch, F. C., & Dekel, A. 2010, MNRAS, 405, 1690
Dutton, A. A., van den Bosch, F. C., Dekel, A., & Courteau, S. 2007, ApJ, 654, 27
Elmegreen, B. G. 1993, ApJ, 411, 170
Elmegreen, B. G. 2002, ApJ, 577, 206
Erb, D. K., Steidel, C. C., Shapley, A. E., Pettini, M., Reddy, N. A., & Adelberger, K. L. 2006, ApJ, 646, 107
Feldmann, R., Gnedin, N. Y., & Kravtsov, A. V. 2010, ApJ, submitted (arXiv:1010.1539)
Firmani, C., & Avila-Reese, V. 2000, MNRAS, 315, 457
Gaensler, B. M., Madsen, G. J., Chatterjee, S., & Mao, S. A. 2008, PASA, 25, 184
Galli, D., & Palla, F. 1998, A&A, 335, 403
Gao, Y., & Solomon, P. M. 2004, ApJ, 606, 271
Gillmon, K., Shull, J. M., Tumlinson, J., & Danforth, C. 2006, ApJ, 636, 891
Glover, S. C. O., & Abel, T. 2008, MNRAS, 388, 1627
Glover, S. C. O., & Mac Low, M. 2007a, ApJS, 169, 239
Glover, S. C. O., & Mac Low, M. 2007b, ApJ, 659, 1317
Gnedin, N. Y., & Abel, T. 2001, New Astron., 6, 437
Gnedin, N. Y., & Kravtsov, A. V. 2010, ApJ, 714, 287
Gnedin, N. Y., Tassis, K., & Kravtsov, A. V. 2009, ApJ, 697, 55
Goldsmith, P. F., & Li, D. 2005, ApJ, 622, 938
Haffner, L. M., et al. 2009, Rev. Mod. Phys., 81, 969
Heyer, M. H., Corbelli, E., Schneider, S. E., & Young, J. S. 2004, ApJ, 602, 723
Hirashita, H. 1999, ApJ, 522, 220
Hoopes, C. G., & Walterbos, R. A. M. 2003, ApJ, 586, 902
Hoopes, C. G., Walterbos, R. A. M., & Rand, R. J. 1999, ApJ, 522, 669
Hui, L., & Gnedin, N. Y. 1997, MNRAS, 292, 27
Inoue, A. K. 2003, PASJ, 55, 901
Kennicutt, R. C., Jr. 1998, ApJ, 498, 541
Kennicutt, R. C., Jr., et al. 2007, ApJ, 671, 333

Kravtsov, A. V. 1999, PhD thesis, New Mexico State Univ.
Kravtsov, A. V. 2003, ApJ, 590, L1
Kravtsov, A. V., Gnedin, O. Y., & Klypin, A. A. 2004, ApJ, 609, 482
Kravtsov, A. V., Klypin, A., & Hoffman, Y. 2002, ApJ, 571, 563
Krumholz, M. R., Ellison, S. L., Prochaska, J. X., & Tumlinson, J. 2009a, ApJ, 701, L12
Krumholz, M. R., & McKee, C. F. 2005, ApJ, 630, 250
Krumholz, M. R., McKee, C. F., & Tumlinson, J. 2008, ApJ, 689, 865
Krumholz, M. R., McKee, C. F., & Tumlinson, J. 2009b, ApJ, 693, 216
Krumholz, M. R., McKee, C. F., & Tumlinson, J. 2009c, ApJ, 699, 850
Krumholz, M. R., & Tan, J. C. 2007, ApJ, 654, 304
Leroy, A., Bolatto, A., Stanimirovic, S., Mizuno, N., Israel, F., & Bot, C. 2007, ApJ, 658, 1027
Lisenfeld, U., & Ferrara, A. 1998, ApJ, 496, 145
Madden, S. C. 2008, in EAS Publ. Ser. 31, Far-Infrared Workshop 2007, ed. C. Kramer, S. Aalto, & R. Simon (Les Ulis: EDP Sciences), 123
Mannucci, F., et al. 2009, MNRAS, 398, 1915
Martin, C. L., & Kennicutt, R. C., Jr. 2001, ApJ, 555, 301
Mateo, M. L. 1998, ARA&A, 36, 435
Mathis, J. S., Mezger, P. G., & Panagia, N. 1983, A&A, 128, 212
Matthews, L. D., Gao, Y., Uson, J. M., & Combes, F. 2005, AJ, 129, 1849
McKee, C. F., & Krumholz, M. R. 2010, ApJ, 709, 308
McKee, C. F., & Ostriker, E. C. 2007, ARA&A, 45, 565
Moster, B. P., Maccio', A. V., Somerville, R. S., Johansson, P. H., & Naab, T. 2010, MNRAS, 403, 1009
Orban, C., Gnedin, O. Y., Weisz, D. R., Skillman, E. D., Dolphin, A. E., & Holtzman, J. A. 2008, ApJ, 686, 1030
Pelupessy, F. I., & Papadopoulos, P. P. 2009, ApJ, 707, 954
Pelupessy, F. I., Papadopoulos, P. P., & van der Werf, P. 2006, ApJ, 645, 1024
Penston, M. V. 1970, ApJ, 162, 771
Rafelski, M., Wolfe, A. M., & Chen, H.-W. 2011, ApJ, submitted (arXiv:1011.6390)
Reynolds, R. J. 1989, ApJ, 339, L29
Reynolds, R. J. 1991, in IAU Symp. 144, The Interstellar Disk-Halo Connection in Galaxies, ed. H. Bloemen (Cambridge: Cambridge Univ. Press), 67
Ricotti, M., Gnedin, N. Y., & Shull, J. M. 2002, ApJ, 575, 33
Robertson, B., Bullock, J. S., Cox, T. J., Di Matteo, T., Hernquist, L., Springel, V., & Yoshida, N. 2006, ApJ, 645, 986
Robertson, B. E., & Kravtsov, A. V. 2008, ApJ, 680, 1083
Robertson, B., Yoshida, N., Springel, V., & Hernquist, L. 2004, ApJ, 606, 32
Rossa, J., & Dettmar, R. 2003, A&A, 406, 493
Roychowdhury, S., Chengalur, J. N., Begum, A., & Karachentsev, I. D. 2009, MNRAS, 397, 1435
Rudd, D. H., Zentner, A. R., & Kravtsov, A. V. 2008, ApJ, 672, 19
Saitoh, T. R., Daisaka, H., Kokubo, E., Makino, J., Okamoto, T., Tomisaka, K., Wada, K., & Yoshida, N. 2008, PASJ, 60, 667
Salim, S., et al. 2007, ApJS, 173, 267
Schaye, J., & Dalla Vecchia, C. 2008, MNRAS, 383, 1210
Schmidt, M. 1959, ApJ, 129, 243
Shapiro, P. R., & Kang, H. 1987, ApJ, 318, 32
Springel, V., & Hernquist, L. 2003, MNRAS, 339, 289
Springel, V., & Hernquist, L. 2005, ApJ, 622, L9
Stahler, S. W., & Palla, F. 2005, The Formation of Stars (Weinheim: Wiley-VCH)
Sutherland, R. S., & Dopita, M. A. 1993, ApJS, 88, 253
Tassis, K. 2007, MNRAS, 382, 1317
Tozzi, P., Madau, P., Meiksin, A., & Rees, M. J. 2000, ApJ, 528, 597
Tumlinson, J., et al. 2002, ApJ, 566, 857
Verley, S., Corbelli, E., Giovanardi, C., & Hunt, L. K. 2010, A&A, 510, A64
Wada, K., & Norman, C. A. 2001, ApJ, 547, 172
Wada, K., & Norman, C. A. 2007, ApJ, 660, 276
Wolfe, A. M., & Chen, H.-W. 2006, ApJ, 652, 981
Wolfire, M. G., McKee, C. F., Hollenbach, D., & Tielens, A. G. G. M. 2003, ApJ, 587, 278
Wolfire, M. G., Tielens, A. G. G. M., Hollenbach, D., & Kaufman, M. J. 2008, ApJ, 680, 384
Wong, T., & Blitz, L. 2002, ApJ, 569, 157
Wu, J., Evans, N. J., II, Gao, Y., Solomon, P. M., Shirley, Y. L., & Vanden Bout, P. A. 2005, ApJ, 635, L173
Wyder, T. K., et al. 2009, ApJ, 696, 1834